To the Graduate Council:

I am submitting herewith a thesis written by Rui Tang entitled "An Appropriate Stiffness Degradation Parameter to Monitor Fatigue Damage Evolution in Composites." I have examined the final paper copy of this thesis for form and content and recommend that it be accepted in partial fulfillment of the requirements for the degree of Master of Science, with a major in Mechanical Engineering.

Y. Jack Weitsman, Major Professor

We have read this thesis
and recommend its acceptance:

John D. Landes, Professor

Madhu S. Madhukar, Associate Professor

Acceptance for the Council:

Vice Provost and Dean of Graduate Studies

An Appropriate Stiffness Degradation Parameter to Monitor Fatigue Damage Evolution in Composites

A Thesis

Presented for the Master of Science

Degree

The University of Tennessee, Knoxville

Rui Tang

May 2003

ACKNOWLEDGEMENTS

I would like to thank Dr. Y. Jack Weitsman, who changed my life by offering the opportunity to study here under his guidance. I have learned from him not only professional expertise, but also his humble personality. I thank Dr. Xiaoming Li, who contributed greatly to this study and offered personal help when it was most needed. I thank Dr John D. Landes and Dr. Madhu S. Madhukar, my graduate committee members, for their advice and suggestion. I would like to thank Dr. Dayakar Penumadu and his PhD student Han Lin, who kindly lent me their equipment and trained me how to use it. I thank Dr. Axinte Ionita for helping me with Finite Element Analysis.

I thank my family and friends, whose encouragements made this work possible.

ABSTRACT

This thesis suggests that torsional stiffness be an effective parameter to monitor internal damage evolution in the forms of transverse cracks and interlaminar delaminations in cross-ply laminates caused by fatigue loading. $[0^0_3/90^0_5]_s$ cross-ply laminates were fabricated from AS4/3501-6 carbon epoxy prepreg with various spacings of interlaminar delaminations, which were simulated by Dupont® Teflon® films. Transverse cracks were introduced by tensile tests. Torsional and tensile tests were conducted to record torsional and tensile stiffness, and correlate their magnitude with damage levels. Finite Element Analysis (FEA) was employed to computationally investigate the above issue by means of a 3-D model that was generated with ANSYS 5.7. Calculation of torsional and longitudinal stiffnesses for laminates of various crack densities and delamination spacings predicted trends similar to those recorded experimentally. Based on both experimental and computational results, it is concluded that torsional stiffness is indeed more effective in indicating fatigue damage evolution in cross-ply laminates than longitudinal stiffness.

TABLE OF CONTENTS

LIST OF TABLES

Table | Page

LIST OF FIGURES

Figure Page

LIST OF FIGURES (CONTINUED)

Chapter 1

Introduction

Fiber reinforced composite materials are being widely utilized in many engineering fields, such as: aircraft, aerospace, civil and automotive structures, sports equipment and biomedical products. The main advantage of composite materials over conventional materials is their high strength and stiffness to weight ratios.

In most circumstances composite materials are formed from individual, unidirectionally reinforced layers (plies). These plies, which consist of a multitude of parallel fibers bonded to each other by a polymeric matrix, are stacked at different orientations, to form a composite material laminate. When such laminates are subjected to static or fatigue loads they develop damage in the forms of profuse cracks or micro-cracks that are usually channeled along the fiber directions within each ply, as well as delaminations at interfaces between adjacent plies. The aforementioned forms of damage usually occur at some sequential order. A significant amount of attention was focused on cross-ply, i.e. $[0^0_m/90^0_n]_s$. For such lay-ups R. Talreja [1] described the damage development under fatigue as multi-staged. The initial stage consists of transverse cracks parallel to fibers in the 90° ply group. The crack number (density) increases at a rate determined by the level of applied stresses and the available fracture energy for further cracking within that ply group. Note that the latter energy depends on the spacing between already existing transverse cracks and on the constraints imposed by the neighboring 0° ply group. At some stage the above spacing reaches saturation, which is a property of the laminate and is independent of loading history. The state of damage given by the saturated and stable pattern of such transverse cracking in a laminate has been termed the "Characteristic Damage State" (CDS) by Reifsnider [2]. At this state of damage the distance between adjacent cracks is approximately uniform. A subsequent stage of damage development is that of interlaminar delamination at the interfaces between the 0° and 90° ply groups. The delaminations develop in a mixed mode fracture. The terminal stage consists usually of large-scale fiber failures in the 0° plies. A schematic picture of damage development is shown in figure 1.1[1] [3].

A substantial amount of research has been done attempting to correlate the level of transverse cracks in cross-ply laminates with the degradation in longitudinal stiffness and employ the latter as an indicator of fatigue life. Highsmith et al. [4] used a shear lag

---

[1] All figures are located in the Appendix.

analysis to predict the longitudinal stiffness reduction. Simplifying assumptions were made that cracks remain sufficiently far apart so that their mutual interaction can be neglected, and that the shear stress developed between the plies is confined within a thin layer of undetermined thickness. Tan and Nuismer [5] modeled the progressive matrix cracking of composite laminates that contain a cracked 90^o ply group and is subject to uniaxial tensile or shear loading using linear elastic fracture mechanics. Closed form solutions were obtained for laminate stiffnesses and Poisson's ratio as functions of crack density. Hashin [6] studied stiffness reduction using a variational approach based on the principle of minimum complementary energy. Lee and Daniel [7] obtained closed form solutions for stress distributions, transverse crack density and reduced stiffnesses of damaged plies as well as the entire laminate as a function of applied load and properties of the constituent plies using a simplified shear lag analysis, where the shear lag parameter is only a function of geometry and shear moduli of the lamina. Erdman and Weitsman [8] investigated the mechanical response of cross-ply SiC/CAS ceramic matrix composites. An extended shear-lag model, which incorporated non-linear behavior of the 0^o plies and interlaminar slip between the 0^o and 90^o plies was employed. The evolution of the multi-cracking process was determined by means of fracture criterion, leading to the prediction of the overall stress-strain response of the cross-ply laminate. The above analyses were supported by experimental findings as well.

All the aforementioned investigation into the correlation between growing damage and longitudinal stiffness showed that, beyond an initial degradation during the earlier stage of loading, the longitudinal stiffness of cross-ply composite laminates is insensitive to stress amplitude or to the number of cycles under tension/tension fatigue. Consequently, this stiffness cannot serve as an adequate measure of damage growth. Figure 1.2 [9] shows that: the longitudinal stiffness drops by about 2% in the initial stage of fatigue loading, following by a long plateau where it stays practically constant before the sudden failure of the specimen. This observation was noted, among others, by Reifsnider [10] and Talreja [3] and was traced to the fact that the longitudinal modulus of cross-ply laminates depends almost entirely on the 0^o plies. Consequently any damage, such as transverse cracking in the 90^o plies and interfacial delaminations, that does not interfere with the performance of the fibers in the 0^o plies will have only a marginal effect on the longitudinal stiffness. To obtain a stronger correlation between damage and stiffness it is necessary to consider an alternate component of the stiffness tensor of higher sensitivity to the damage at hand, i.e. transverse crack and interlaminar delamination. In this thesis, it is suggested that the torsional stiffness of laminated composites can play such a role.

Experimental tests were conducted on cross-ply carbon-epoxy laminates with transverse cracks and interlaminar delamination of various densities, recording their longitudinal and torsional stiffness. Based on these results, correlation between internal damage level and degradation of these two stiffnesses were examined. A Finite Element Analysis was performed to compare computational with experimental results. It is concluded that torsional stiffness is indeed a much more sensitive indicator for the level of both transverse cracks and interlaminar delaminations in cross-ply laminates than the longitudinal stiffness.

Chapter 2

Material Properties Tests

2.1 Introduction

This chapter concerns the experimental determination of material properties for the AS4/3501-6 carbon epoxy composite material used in subsequent studies. For this purpose, tensile tests were performed on AS4/3501-6 laminates of both unidirectional and cross-ply ($[\pm45^0]_4$) lay-ups, and their stress-strain responses were examined. Totally 5 parameters were determined: longitudinal modulus E_1, transverse modulus E_2, major Poisson's ratio ν_{12}, minor Poisson's ratio ν_{21} and in-plane shear modulus G_{12}. Longitudinal and transverse tensile strength F_{1t} and F_{2t}, as well as ultimate longitudinal and transverse tensile strain ε_{1t}^u and ε_{2t}^u were also obtained.

2.2 Procedure

Hercules carbon prepreg tapes AS4/3501-6, which is amine-cured epoxy resin reinforced with unidirectional carbon fibers, were used to fabricate the composite laminates. After cutting the tapes into 12×12 inches sheets, these sheets were laid in desired angles. A glass cylinder was firmly pushed across the laminates in order to squeeze out any air that may have been trapped between individual layers. Finally, upon completion of the entire laminate lay-up, it was placed into an OEM composite curing system and cured according to the user-specified program. In this curing procedure, the maximum temperature was 350 °C and total curing time was 328 minutes. Figure 2.1 and 2.2 show the OEM composite curing system and a laminate contained within it after curing, respectively.

The cured laminates were then cut into coupons with MSC Surface Grinder. Geometric dimensions for all the specimen coupons were 8×1 inches in accordance with ASTM standards [11]. Glass-epoxy tabs were adhesively bonded to both surfaces at the two opposite edges of each coupon. Two strain gages, M-M EA-06-250AE-350, manufactured by Measurements Group Inc., were applied in longitudinal and transverse directions respectively at the geometric center on the surface of each specimen. Cross-sectional dimensions, namely width and thickness of each specimen were measured at 5 different positions along the coupon's length. Figure 2.3 shows the dimensions of the specimens. Figure 2.4 is a picture of a tabbed specimen. Figure 2.5 gives a closer look at the two strain gages.

Totally three lay-ups were prepared: $[0^\circ]_6$, $[90^\circ]_{12}$ and $[\pm 45^\circ]_4$. The $[0^\circ]_6$

specimens were tested to determine the longitudinal young's modulus E_1 and major Poisson's ratio ν_{12}, while the $[90°]_{12}$ coupons were used for the transverse Young's modulus E_2 and minor Poisson's ratio ν_{21}. Data from $[\pm 45°]_4$ specimens were used to calculate in-plane shear modulus G_{12}. Six specimens of each lay-up were manufactured and then tested.

An 810 Material Test System (MTS) with 647 Hydraulic Wedge Grip of 100KN force capacity was used to conduct the tests. All the tensile tests were set in displacement control mode at the loading rate of 1mm/sec without interruption until specimen failure. Data of axial tensile load and strains in both longitudinal and transverse directions were collected at increment of 0.1 second via an automatic data acquisition system. Figure 2.6 depicts a specimen tested in tension on the MTS machine.

2.3 Data Reduction

The axial tensile load data were converted to axial stress using the cross-sectional dimensions recorded before by $\sigma = P/A$. The formulas used to calculate the material properties follow.

Modulus:

$$E_1 = \frac{\sigma_1}{\varepsilon_1}, \quad E_2 = \frac{\sigma_2}{\varepsilon_2}$$

Poisson's ratio:

$$\nu_{12} = -\frac{\varepsilon_2}{\varepsilon_1}, \quad \nu_{21} = -\frac{\varepsilon_1}{\varepsilon_2}$$

Shear modulus:

$$G_{12} = \frac{\bar{\sigma}_x}{2(\bar{\varepsilon}_x - \bar{\varepsilon}_y)},$$

where $\bar{\varepsilon}_x$ and $\bar{\varepsilon}_y$ are the axial and transverse strains of the $[\pm 45^\circ]_4$ specimens, respectively [12].

All the aforementioned were evaluated from the slope of a line fitted into a suitably corresponding plot (stress-strain or strain-strain) from the recorded data points by Least Square method. The ultimate stress and strain were recorded as well.

Typical stress-strain plots for each of the three groups of specimens are shown in the following figure 2.7, 2.8 and 2.9. In figure 2.9, "shear stress" and "shear strain" refers to $\frac{\bar{\sigma}_x}{2}$ and $(\bar{\varepsilon}_x - \bar{\varepsilon}_y)$ respectively. Note that the curve becomes non-linear beyond a certain stress level. Only the linear portion of that curve was used for calculating the in-plane shear modulus G_{12}. As expected, the stress-strain response for $[0^\circ]_6$ and $[90^\circ]_{12}$ specimen remains linear until the approach of failure.

2.4 Results

Table 2.1 summarizes the experimentally determined material properties for AS4/3501-6 carbon epoxy composite material.

Table 2.1 Material properties for AS4/3501-6 carbon epoxy composite material

	E_1 GPa	E_2 GPa	G_{12} GPa	ν_{12} mm/mm	ν_{21} mm/mm	F_{1t} MPa	F_{2t} MPa	ε_{1t}^{u} %	ε_{2t}^{u} %
	159.3	8.16	5.17	0.33	0.0193	2460.8	39.37	1.57	0.50
	160.8	8.17	5.10	0.31	0.0117	2503.4	29.35	1.61	0.36
	146.7	8.38	5.43	0.31	0.0149	2394.0	46.31	1.60	0.56
	151.7	8.63	5.10	0.30	0.0157	2368.3	53.22	1.53	0.63
	151.0	8.74	5.31	0.40	0.0186	2642.6	52.78	1.64	0.62
Avg.	153.6	8.44	5.22	0.32	0.0159	2473.8	44.21	1.59	0.53
STD*	5.96	0.26	0.14	0.04	0.003	108.4	10.0	0.04	0.11

* STD = standard deviation

Chapter 3

Edge Effect Analysis

3.1 Introduction

In order to experimentally study the correlation between the level of internal damage in a cross-ply laminate and degradation of the torsional stiffness, a delaminating torsional specimen (DTS) need to be designed for this purpose, see figure 3.1. Teflon films were to be inserted in various locations of the specimen to simulate delaminations as desired. During the twisting test, the specimen would be clamped at both ends, with one end fixed and the twisting torque imposed from the other. The dimensions of the specimen and minimum distance of the inserted Teflon film from the ends have to be well designed such that the edge effects from the applied torque and constraints at the ends of the specimen will not interfere with the stress fields of the delaminated part within the interior part of the specimen. Such a circumstance implies that stress and displacement profiles are to remain independent of the length coordinate z within the above-mentioned interior domain.

This chapter presents a Finite Element Analysis (FEA) of the edge effects caused by an applied torque at one end of the coupon and geometric constraints at the other end. The results of the analysis verify that the configuration of DTS specimen and its dimensions, presented in the previous chapter yield valid experimental results.

3.2 Computational Scheme

A 3-D model was developed employing ANSYS 5.7 [13] and utilizing SOLID45 elements. Linear elastic behavior was assumed throughout. The configuration of the specimen is shown in figure 3.1, which corresponds to a $[0^0_2/90^0_4]_s$ lay-up with ply thickness of 0.125 mm. The planar dimensions of the specimen are 228.6mm × 25.4mm. Meshing was achieved by dividing the specimen's width (x direction) into 8 equal parts, with the thickness of 90° ply group further subdivided into four equal portions. The element lengths (z direction) were 1.27 mm within the end regions of lengths 12.7 mm and 6.35 mm from the geometrically constrained end and loading end, respectively (portion AB and EF in figure 3.2). These end zones were chosen in order to examine the edge effects employing fine mesh elements. The element lengths in the interior region that starts from z = 63.5 mm to the mid-cross-section were 1.27 mm as well (portion CD in figure 3.2). This arrangement was selected because the stress distribution of a bar of solid section is symmetric about the mid-cross-section. The lengths of elements between z = 12.7 mm and 63.5 mm were 2.54 mm (portion DF in figure 3.2). The lengths of the remaining of elements (portion BC in figure 3.2) were 7.62 mm. Figure 3.2 shows the elements of the model.

As experimentally determined in Chapter 2, the elastic constants for the material are as following: E_1 = 153.6 GPa, E_2 = 8.44 GPa, G_{12} = 5.22 GPa, ν_{12} = 0.32 and ν_{21} = 0.0159. Poisson's ratio ν_{23} = 0.59 and shear modulus G_{23} = 3.17 GPa for AS4/3501-6 were taken from reference [12]. Engineering constants for 0° ply group and 90° ply group are transformed from material properties by [12]:

$$\frac{1}{E_x} = \frac{m^2}{E_1}\left(m^2 - n^2\nu_{12}\right) + \frac{n^2}{E_2}\left(n^2 - m^2\nu_{21}\right) + \frac{m^2n^2}{G_{12}}$$

$$\frac{1}{E_y} = \frac{n^2}{E_1}\left(n^2 - m^2\nu_{12}\right) + \frac{m^2}{E_2}\left(m^2 - n^2\nu_{21}\right) + \frac{m^2n^2}{G_{12}}$$

$$\frac{1}{G_{xy}} = \frac{4m^2n^2}{E_1}\left(1 + \nu_{12}\right) + \frac{4m^2n^2}{E_2}\left(1 + \nu_{21}\right) + \frac{\left(m^2 - n^2\right)^2}{G_{12}}$$

In the above formulas, m = *cos*θ, n = *sin*θ, where the angle θ is measured positive counterclockwise from the *x*-axis to the fiber direction. Consequently, for the current lay-up one has:

For 0° ply group: θ = 0°

E_x = 153.6 GPa, $E_y = E_z$ = 8.44 GPa, $G_{xy} = G_{xz}$ = 5.22 GPa, G_{yz} = 3.17 Gpa, $\nu_{xy} = \nu_{xz}$ = 0.32, ν_{yz} = 0.59

For 90° ply group: $\theta = 90°$

$E_x = E_z == 8.44$ GPa, $E_y = 153.6$ GPa, $G_{xy} = G_{yz} = 5.22$ GPa, $G_{xz} = 3.17$ Gpa, $\nu_{xy} = 0.0159$, $\nu_{yz} = 0.32$, $\nu_{xz} = 0.59$

All the nodes at the left end, where z = 0, are constrained in all degree of freedom. Twisting loading was introduced by applying a rotational displacement on nodes at the right end, where z = 228.6 mm, or 9 inches. The rotational displacement, which is equivalent to a twisting angle of 25° on the right end, is implemented by a displacement function that defines the displacements in both x and y direction of each node to be a function of its distance to the geometric center of the right end surface. The displacement in the z direction of all the nodes at the loading end was not specified, but was subject to the requirement of null net axial load, which simulated the actual testing condition.

All evaluated stress and displacement components at 8 different cross sections were examined. These cross sections are at: z = 0 (constrained end), 1, 3, 4, 4.5 (mid-section), 6, 8 and 9 (loading end) inches.

3.3 Results

Figures 3.3 through 3.11 show the stress and displacement distributions in the 8 above mentioned cross sections, respectively. In the above figures, all the stress and displacement components were normalized by the amplitude of the effective torque, which was calculated from the reaction forces at both loaded and constrained ends.

These figures demonstrate that the distributions of all the stress and displacement components over the cross section remain independent of the location z, except near the loaded and the constrained ends. In addition, it can be noted from figure 3.7 that sufficiently far from both the coupon's ends, τ_{xz} varies linearly with respect to y, except for edge effects near the sample's ends. These results appear to be consistent with the analytical solution for homogeneous prismatic bars of thin rectangle cross-section subjected to torsion given in [14]:

$$\tau_{xz} = -2y \cdot \frac{M_t}{J}$$

From the distribution of normal stresses σ_x, σ_y and σ_z, it is found that the edge effects are significant at both ends. But this effect does not extend to the central part, i.e. $1 \leq z < 6$ inches. For the shear stresses τ_{xy} the edge effect is confined to the exterior regions alone and $\tau_{xy} \approx 0$ in the interior zone, as may have been expected. Regarding the displacements, figures 3.9 - 3.11 show that u_x varies linearly with y, u_y varies linearly with x, and $u_z \approx 0$ over the entire length of the coupon with no discernible edge effects. It may thus be concluded that to exclude edge effect, interlaminar delaminations should be embedded within the region that is 1 inch away from the constrained end and 2 inches away from the loading end.

Chapter 4

Torsion Test

4.1 Introduction

The purpose of this chapter is to experimentally investigate the effects of transverse cracks and delamination on torsional stiffness of Hercules AS4/3501-6 $[0^0_3/90^0_5]_S$ cross-ply laminates. Experimental methods were employed to simulate internal damage in the laminates, such as caused by tensile fatigue loading.

It is well known that when cross-ply samples, as well as other lay-ups, are subjected to either monotonically increasing loads or to cyclic fatigue, they develop internal damage in the form of transverse cracks of increasing density in the 90° ply groups. Upon reaching a certain asymptotic value, further exposure to external loads results in the initiation and growth of interlaminar delaminations at the 0° /90° interfaces, eventually leading to a rather abrupt final failure. In the present study, such delaminations were introduced artificially as pre-determined spacings and locations along the specimens.

4.2 Procedure

The procedure of fabricating the $[0^0_3/90^0_5]_s$ laminates was the same as described in chapter 2, except for the introduction of delaminations. Since it is impossible to control the size and location of delamination when conducting tensile fatigue tests on cross-ply laminates, it was decided to simulate their presence by the insertion of Dupont® Teflon® films. The purpose of the anti-stick Teflon film is to maintain the separation between two adjacent prepreg layers during the curing process, thus simulating the presence of delamination at the location of the Teflon film. Dupont FEP Fluorocarbon Film 50 A of 12.5 μm thickness was used. The film, which was shipped in width of 15 in, was placed between two sheets of paper. This "assembly" was subsequently cut into 2 mm wide strips. The Teflon film strips were then laid symmetrically between the 0° ply groups and 90° ply groups over a 5 inch long central portion of the laminate, leaving undelaminated regions of 2.5 inch and 3.5 inch lengths, respectively, at the two ends of the plate, as determined in chapter 3. Three sets of laminates were thus made with various spacing of Teflon film strips to simulate delaminations of various densities. These spacings were 2mm, 4mm and 12mm, respectively. A set of specimens without Teflon film was prepared for purpose of comparison. The laminated plates were cut into 11×1 inch coupons. Like in previous tensile experiments, glass-epoxy tabs were adhesively bonded to both surfaces at two opposite edges of the each coupon. A strain gage, M-M

EA-06-250AE-350 manufactured by Measurements Group Inc., was attached in the longitudinal direction at the geometric center on the surface of each specimen. Cross-sectional dimensions, namely width and thickness, of each specimen were measured at 5 different positions along the length. Figure 4.1 depicts the cutting process of Teflon film. Figure 4.2 shows a single sheet of AS4/3501-6 prepreg with a Teflon film strip laid on it.

Transverse cracks in 90^o ply groups within the cross ply coupons were introduced through tensile loads, which were conducted on an 810 Material Test System (MTS) with 647 Hydraulic Wedge Grip of 100KN force capacity in displacement control mode at 1mm/min. The first test, on one sample from each set, was intended to get the tensile strength. When the linear stress-strain plot began to reach a plateau, tests were immediately stopped and the plateau level stress was considered to be the tensile strength for that set of specimens. Different transverse crack densities were obtained by subjecting the remaining specimens to tensile stresses of various levels, proportionately to the above-mentioned tensile strength. Hewlett Packard 43804N X-Ray system and Polaroid Black &. White Instant Sheet Film Polapan Type 52 (ISO 400) were used to obtain X-radiographs of the specimens and thus examine the transverse crack densities. (The recipe for the X-Ray dye penetrant is as: dissolve 60 grams of ZnI_2 in 10 ml each of water, Isopropyl/Alcohol and Kodak Photo-Flo 200. The KVP setting for the X-Ray system was 21 and exposure time was 0.8 minutes.) From the X-radiographs, it was possible to count the number of transverse cracks and determine an average transverse crack density by dividing their number by the length of specimen. In this manner several sets of specimens varying in the densities of transverse crack and interlaminar delamination were readied for torsional test. It is worth noting that no delamination was introduced by tensile tests. Figure 4.3 depicts the Hewlett Packard 43804N X-Ray system. Figure 4.4 shows a typical X-radiograph of a specimen containing transverse cracks. Such cracks are shown by the dark vertical lines in that figure.

An 859 Material Test System (MTS) with 647 Hydraulic Wedge Grip of 31KN static force capacity was used for the torsion tests. The specimens were clamped at both ends. The top was fixed and the twisting torque was applied from the bottom grip. At the loading end, the axial displacement in vertical direction was unconstrained, while the load in that direction was maintained at zero level to ascertain pure twist. The precision of angle displacement measurement is 0.25% of the total capable range of $\pm 14^{o}$, namely $\pm 0.035^{o}$. All the torsion tests were programmed in twisting angle control mode at the loading rate of 1^{o}/min. The total applied angular displacement was 20^{o} to avoid additional damage to the specimen due to torsion. Twisting torque and angle displacement data were collected at 1-second increments via an automatic data acquisition system. A specimen subjected to torsion is shown in figure 4.5.

4.3 Data Reduction

The axial tensile load data from the preliminary tensile tests were converted to axial stress through division by cross-sectional area. Then the longitudinal stiffness for each specimen was obtained from the stress-strain plot.

The twisting angle φ was converted to relative angle through division by the length l of specimen. The torsional stiffness was calculated as $G = \frac{(Pw)}{\varphi / l}$, where "$Pw$" is the twisting torque. The torsional stiffness was evaluated from the slope of a line fitted to plot of the twisting-moment vs. angle data points by the Least Square method. A typical twisting-moment vs. angle plot is shown in figure 4.6.

4.4 Results

Tables 4.1 through 4.4 summarize the results of the preliminary tensile tests, observed transverse crack density and twisting tests.

Table 4.1 No-delamination set

End load, MPa	0	339.9	340.1	450.56	758.3	758.0
% of Tensile Strength	0	44.8	44.9	59.4	100	100
# of cracks/cm	0	2.11	4.50	5.35	7.23	7.52
E, MPa	N/A	65.5	62.8	64.3	65.8	64.2
G, N·m·m	0.5102	0.5189	0.5039	0.5040	0.4921	0.4656
G/G_o	1	1.0171	0.9878	0.9939	0.9645	0.9126

Table 4.2 2mm-spaced delamination set

End load, MPa	0	333.9	453.8	746.5	750.4
% of Tensile Strength	0	44.5	59.9	100	100
# of cracks/cm	0	2.99	3.14	3.95	4.21
E, GPa	N/A	64.2	63.0	61.9	60.8
G, N·m·m	0.4788	0.4492	0.4748	0.4228	0.4119
G/G_o	0.9385	0.8804	0.9306	0.8287	0.7877

Table 4.3 4mm-spaced delamination set

End load, MPa	0	299.2	343.9	450.8	559.9	744.8
% of Tensile Strength	0	30.8	46.2	60.5	75.2	100
# of cracks/cm	0	1.96	2.65	4.17	4.53	5.73
E, MPa	N/A	60.8	59.7	58.1	61.2	61.7
G, N·m·m	0.4939	0.4870	0.4573	0.4540	0.4287	0.4153
Relative G	0.9681	0.9545	0.8963	0.8898	0.8403	0.8140

Table 4.4 12mm-spaced delamination set

End load, MPa	0	346.5	229.67	457.1	753.6
% of Tensile Strength	0	46.0	30.5	60.7	100
# of cracks/cm	0	2.25	2.77	4.328	7.19
E, GPa	N/A	64.8	63.0	62.7	61.2
G, N·m·m	0.4368	0.4714	0.4685	0.4976	0.4312
G/G_0	0.8561	0.9240	0.9183	0.9753	0.8452

In the above tables, each column represents an individual specimen. The first row, "End load" denotes the tensile stress applied to the specimen. "# of cracks/cm" is the transverse crack density in number of cracks per centimeter. "G/G_0" is the values of torsional stiffness divided by that of a damage-free specimen (namely, no transverse cracks and no delaminations), which readily shows the degradation in torsional stiffness due to internal damage.

Figure 4.7 demonstrates the effects of transverse cracks and delamination on torsional stiffness. The first point on the 12mm spacing curve is abnormally low, which may be due to the fact that it was the first experimental result obtained after changing the grips.

Figure 4.8 shows the effects of transverse cracks and delamination on longitudinal stiffness, relatively to that of the specimen with the least crack density and no delamination. Since specimens with no transverse crack were not tensile tested, their longitudinal stiffnesses are not available.

4.5 Conclusion

Figure 4.7 demonstrates that the torsional stiffness of the coupons at hand reduces with increasing delamination and transverse crack densities. These two trends are clearly exhibited by the four curves despite some inevitable fluctuation of certain data points. This suggests that the torsional stiffness is more sensitive to the presence and density of interlaminar delaminations than longitudinal stiffness. The decrease in torsional stiffness for the specimen with 2-mm spacing delamination and transverse crack of 4.21/cm is 21.2%.

In comparison, figure 4.8 shows no clear relationship between the internal damage level in laminates and the degradation in longitudinal stiffness. Furthermore, even when such degradations do occur they are largely confined to within 6%.

It may therefore concluded that the torsional stiffness is a much more sensitive indicator for the presence of internal damage in cross-ply laminates than the longitudinal stiffness.

Chapter 5

Finite Element Analysis of Stiffness Reduction

5.1 Introduction

In previous chapters, torsional and longitudinal stiffness of cross-ply laminates with internal damage of various levels were obtained by torsional and tensile tests. Relationship of stiffnesses degradation versus damage level was established from experimental findings. The purpose of this chapter is to model the stiffness degradation of the $[0^0_3/90^0_5]_S$ lay-up cross-ply laminate under torsional and tensile using Finite Element Analysis and compare the computational values with the experimental results.

5.2 Computational Scheme

A 3-D model was built with ANSYS 5.7[13], utilizing SOLID45 elements. Linear elastic behavior was assumed throughout. The configuration of the model is shown in figure 5.1. The lay-up was $[0^0_3/90^0_5]_S$ with ply thickness of 0.130 mm, which is the average value measured from actual specimens. The planar dimensions of the specimen are 74mm × 25.4mm. To facilitate the computational effort, as well as to avoid redundant complexities caused by edge effects, the damaged region has been confined to the central

14 mm portion of the coupon, as depicted in figure 5.1. Material properties are as determined in Chapter 3:

For 0^o ply group: $\theta = 0^o$

E_x = 153.6 GPa, $E_y = E_z$ = 8.44 GPa, $G_{xy} = G_{xz}$ = 5.22 GPa, G_{yz} = 3.17 GPa, $\nu_{xy} = \nu_{xz}$ = 0.32, ν_{yz} = 0.59

For 90^o ply group: $\theta = 90^o$

$E_x = E_z$ == 8.44 GPa, E_y = 153.6 GPa, $G_{xy} = G_{yz}$ = 5.22 GPa, G_{xz} = 3.17 Gpa, ν_{xy} = 0.0159, ν_{yz} = 0.32, ν_{xz} = 0.59

Torsion was introduced by subjecting the opposing corners of the right-end edge to a couple of equal and opposite vertical forces of 100 N each, with clamping considered at the left edge. Meshing was achieved by dividing the specimen's width (x direction) into 8 equal parts, with the thickness of 90^o ply group further subdivided into four equal portions. Meshing within the damaged region varies for different delamination spacing, which is denoted by d/e, where 2d is the width of delamination area and 2e is the distance between two adjacent transverse cracks, as illustrated in figure 5.5. For all cases, 2e = 2mm, which is assumed to represent the "Characteristic Damage State" (CDS). For d/e = 0.25, 0.5 and 0.75, the distance between each pair of adjacent cracks were equally divided into 8 portions. For the purpose to compare with experimental data, two additional models with d/e = 1/3 or 1/7 were studied, which correspond to 2mm-spacing and 12mm-spacing delamination sets of specimens, respectively. For these two modes, there are 6 elements in the distance between each pair of adjacent cracks. Both transverse cracks and interlaminar delaminations were introduced by node release. Figure 5.2 shows the elements of the model.

In the model, potential contact and interpenetration of opposite crack faces, in both transverse cracks and delaminations, have been taken into account. No interpenetration was allowed across contacting crack and delamination surfaces, with frictionless contact assumed to exist in those circumstances where opposing crack faces became compressed together. Contact elements CONTA173 and TARGE170 were created on each of the pairs of surfaces that could possibly penetrate each other, respectively.

The sample was considered to be clamped at its left end. Longitudinal (tensile) loading was introduced by imposing a uniform unit longitudinal displacement, and thereby its associated normal force F. As noted earlier, torsion was introduced by subjecting the opposing corners of the right-end edge to equal and opposite vertical loads of P=100N each.

Relative twist due to external torsion was determined by computing the angle

$\Delta\varphi = \varphi_{AA'} - \varphi_{BB'}$ over the length l of the damage zone and relative extension of that same zone was evaluated from $\Delta l = u_{AA'} - u_{BB'}$. Consequently, upon confining attention to the inner damaged portion of length l, it was possible to calculate the relative torsional and longitudinal stiffnesses as follows

$$G = \frac{(Pw)\cdot l}{\Delta\varphi} \quad (1)$$

$$E = \frac{F/(wt)}{\Delta l / l} \quad (2)$$

Clearly, degradations in G and E are inversely proportional to the increase in the values of $\Delta\varphi$ and Δl, respectively.

5.3 Results

Typical distributions of compressive stresses, due to the application of torque, across the contacted portions of both transverse cracks and delamination areas are shown in figure 5.3 and 5.4, respectively. Subsequent computations of twist angles $\Delta\varphi$ and elongations Δl for each of the seven geometries depicted in figure 5.5 yielded values of G and E according to equations (1) and (2), whose normalized magnitudes – relative to their values in the absence of damage – are drawn in figure 5.6 and listed in table 5.1.

Note that the degradation in E/E_0, in the amount of 4.5%, is confined to the stage of increasing transverse crack density, with no further perceptible reduction in that stiffness

Table 5.1 Twist and tensile stiffnesses (E/E_0 and G/G_0, respectively) as a function of damage extent, computed by 3-D FEA with contact simulation

Case	Damage description	E/E_0	G/G_0
1	No damage	1	1
2	1 crack + d/e = 0	0.994	0.997
3	3 cracks+ d/e = 0	0.982	0.992
4	7 cracks + d/e = 0	0.964	0.982
5	7 cracks + d/e = 0.25	0.957	0.939
6	7 cracks + d/e = 0.5	0.948	0.886
7	7 cracks + d/e = 0.75	0.941	0.791

ratio taking place beyond the initiation and upon the growth of delaminations. In contrast, the ratio G/G_0, which diminished by about the same amount as E/E_0 during the advent of transverse crack density, continues to degrade by an additional amount of 21% with the onset and propagation of delaminations.

These FEA solutions for the degradation of the torsional stiffness were presented by the four sets of different delamination spacing with experimental results for comparison in figure 5.7 (a) - (d). It can be seen that the FEA results of normalized torsional stiffness are in good agreement with the experimental data. It is worth noting that in the experiments, both locations and sizes of the delaminations were introduced in advance while transverse cracks developed under external loads occurred at random locations. On the other hand, the computations were performed for transverse cracks that were spaced at equal distances and the spanned opposite delaminati ons, as shown in figure 5.5.

5.4 Conclusion

In this chapter, a 3-D Finite Element Analysis model was generated to study the stiffness degradation of $[0_3^0/90_5^0]_s$ lay-up laminates through a computational approach. Torsional and longitudinal stiffnesses were calculated at various damage levels. The results indicate that the longitudinal stiffness is insensitive to the onset and advent of delaminations. In contrast, the torsional stiffness is indeed more effective in monitoring fatigue damage evolution, especially beyond the initiation and upon the growth of interlaminar delaminations. FEA solutions were compared with experimental results, and were found to be in good agreement with each other.

Chapter 6

Summary and Conclusion

In this thesis, it is suggested that the torsional stiffness of cross-ply laminated composites would be an effective measure for the presence and evolution of internal damage in the forms of transverse cracks and interlaminar delaminations, such as caused by fatigue loading. This effect was investigated through experimental and computational approaches.

Laminates of $[0^\circ]_6$, $[90^\circ]_{12}$ and $[\pm 45^\circ]_4$ lay-up were fabricated from AS4/3501-6 carbon epoxy prepreg and then tensile tested to obtain the principal materials properties. Consistent engineering constants were obtained from replicate specimens. Subsequently, $[0_3^0/90_5^0]_s$ laminates of the same material were fabricated with various spacings of pre-positioned interlaminar delaminations, which were simulated by means of Dupont® Teflon® films. Transverse cracks were introduced by tensile tests. These specimens were then subjected to torsional tests to obtain their torsional stiffness. Based on the experimental data, correlations between degradation in stiffness and damage level were studied. It was found that torsional stiffness was highly sensitive to the presence and density of transverse cracks and interlaminar delaminations, while no clear relationship existed between the level of internal damage in laminates and the degradation in longitudinal stiffness.

A computational method was employed to investigate this problem as well. A 3-D model was generated with ANSYS 5.7 and the torsional and longitudinal stiffnesses for laminates of various crack densities and delamination spacings were calculated. Contact and the issue of inter-penetration of opposing delamination surfaces were addressed. Examination of the results further confirmed the experimental findings. Comparison of FEA solution and experimental data showed that they were in good agreement with each other.

In conclusion, it has been demonstrated that the longitudinal stiffness of cross-ply laminates is insensitive to the onset and advent of delaminations, and therefore cannot serve as a measure for either residual fatigue life or residual strength of these materials. In contrast, the torsional stiffness of the above laminates continues to degrade measurably with both aforementioned forms of damage, namely, a marked decrease during the preliminary stage of increasing transverse crack density is followed by a similar decrease during the later stage of delamination growth. Consequently, reductions in the torsional

LIST OF REFERENCES

1. Talreja, R. "Damage characterization." Fatigue of Composite Materials, Reifsinider, K.L. ed., Amsterdam: Elsevier. (1991) 79 – 103

2. Reifsnider, K.L., et al. "Damage mechanics and NDE of composite laminates." Mechanics of Composite Materials, Recent Advances, Z. Hashin and C.T. Herakovich, eds., New York: Pergamon Press, (1983) 399 – 420

3. Talreja, R. Fatigue of Composite Materials, Technomic Publishing Company, Inc. 1987

4. Highsmith, A.L., Reifsnider, K.L. "Stiffness reduction mechanisms in composite laminates." Damage in Composite Materials. ASTM STP 775. Reifsnider, K.L. ed., American Society for Testing and Materials. (1982) 103 – 117

5. Tan, S.C., Nuismer, R.J. "A theory for progressive matrix cracking in composite laminates" Journal of Composite Materials, (1989) 23: 1029 - 1047

6. Hashin, Z. "Analysis of cracked laminates: a variational approach." Mechanics of Materials, (1985) 4:121 - 136

7. Lee, J.W., Daniel, I.M. "Progressive transverse cracking of crossply composite laminates." Journal of Composite Materials, (1990) 24: 1225 – 1243

8. Erdman, D.L., Weitsman, Y. "The multi-fracture response of cross-ply ceramic composites." International Journal of Solids and Structures, (1998) Vol. 35, No. 36: 5051 – 5083

9. Stinchcomb, W.W., Bakis, C.E. "Chapter 4: Fatigue behaviour of composite laminates." Fatigue of Composite Materials, Reifsnider, K.L. ed, Elsevier. (1991) 162

10. Reifsinider, K.L. "Damage and damage mechanics" Fatigue of Composite Materials, Reifsinider, K.L. ed., Amsterdam: Elsevier. (1991) 11 – 77

11. Adams, D.F., Carlsson, L.A. and Pipes, R.B., Experimental Characterization of Advanced Composite Materials, 3rd Edition, 2003

12. Daniel, I.M., Ishai, O., Engineering Mechanics of Composite Materials, Oxford University Press, 1994

13. ANSYS 5.7.1 HELP, SAS IP, Inc. 2001

14. Herakovich, C.T., Mechanics of Fibrous Composites, John Wiley & Sons, Inc., 1998

APPENDIX

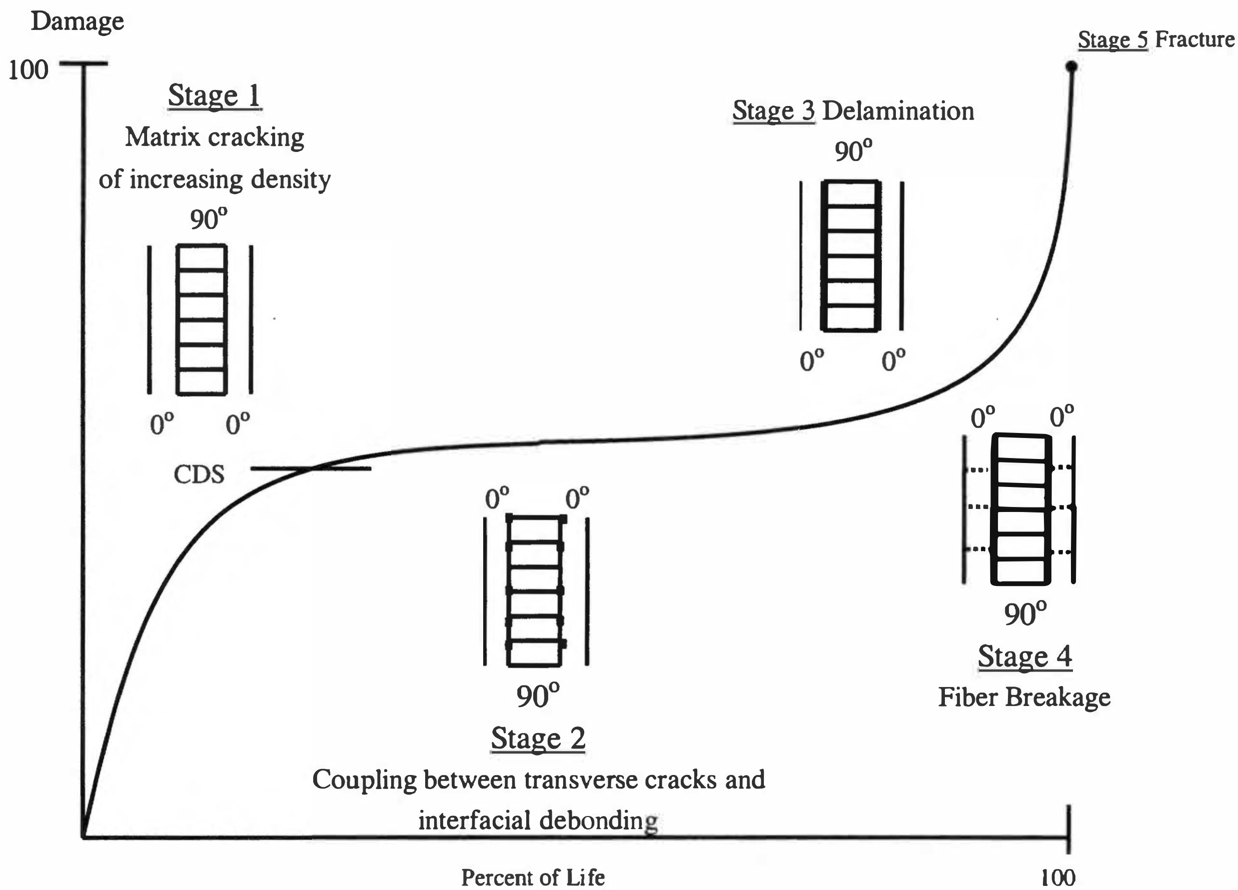

Figure 1.1 A schematic outline of the development of fatigue damage in laminates

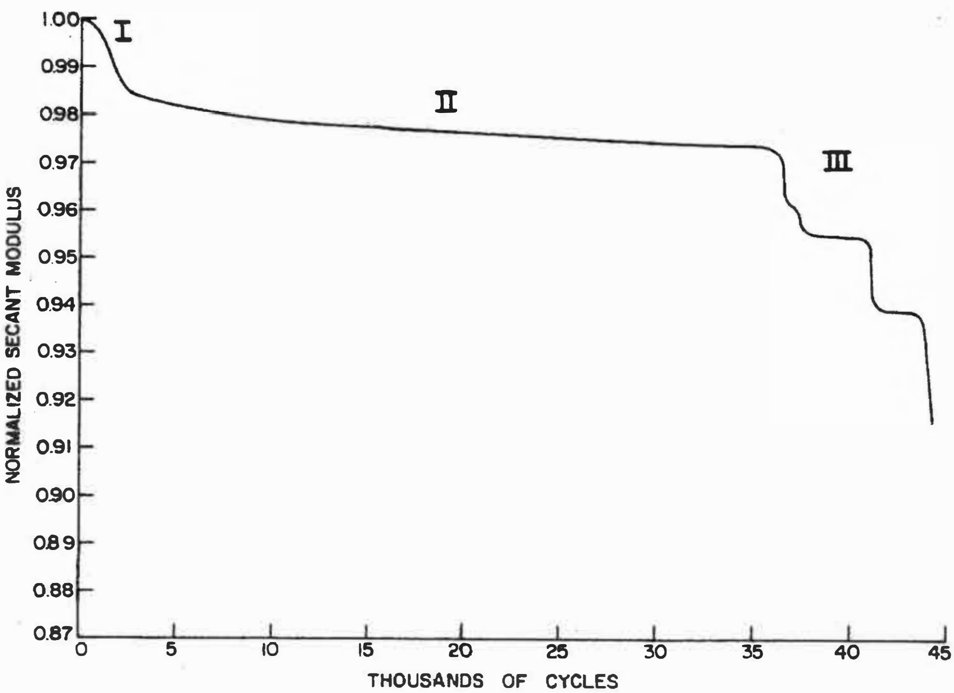

Fig 1.2 Stages of stiffness reduction during fatigue life of a $[0/90_2]_S$ graphite epoxy laminate

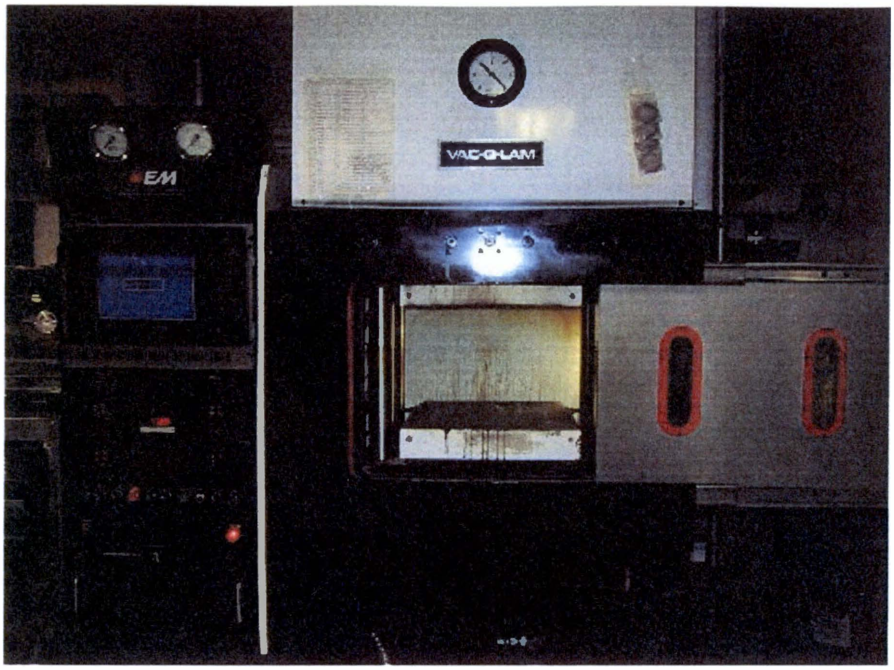

Figure 2.1 OEM composite curing system

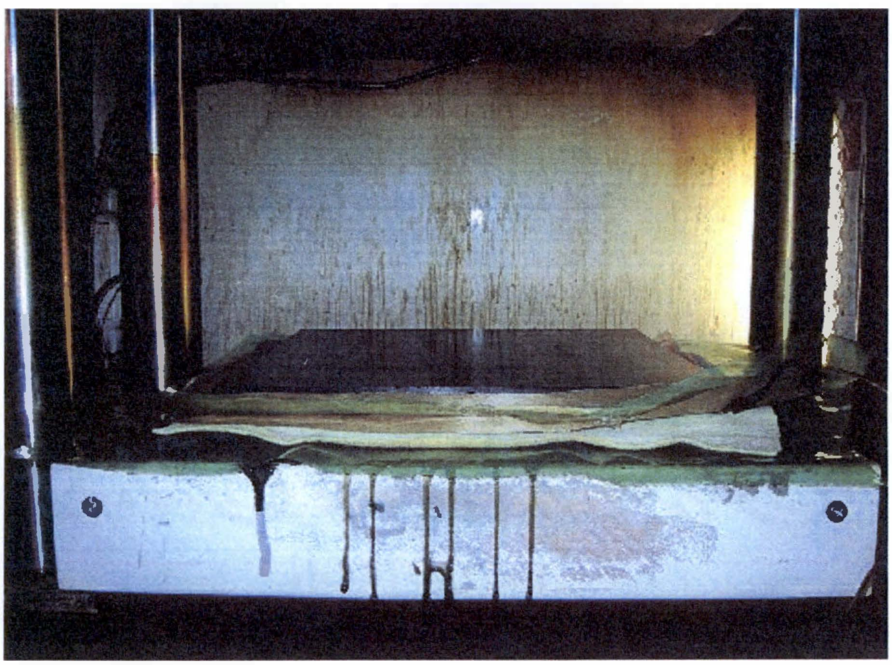

Figure 2.2 A laminate inside the curing system

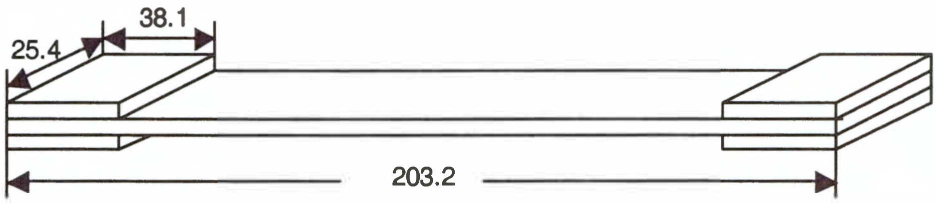

Figure 2.3 Dimensions of specimens (in mm)

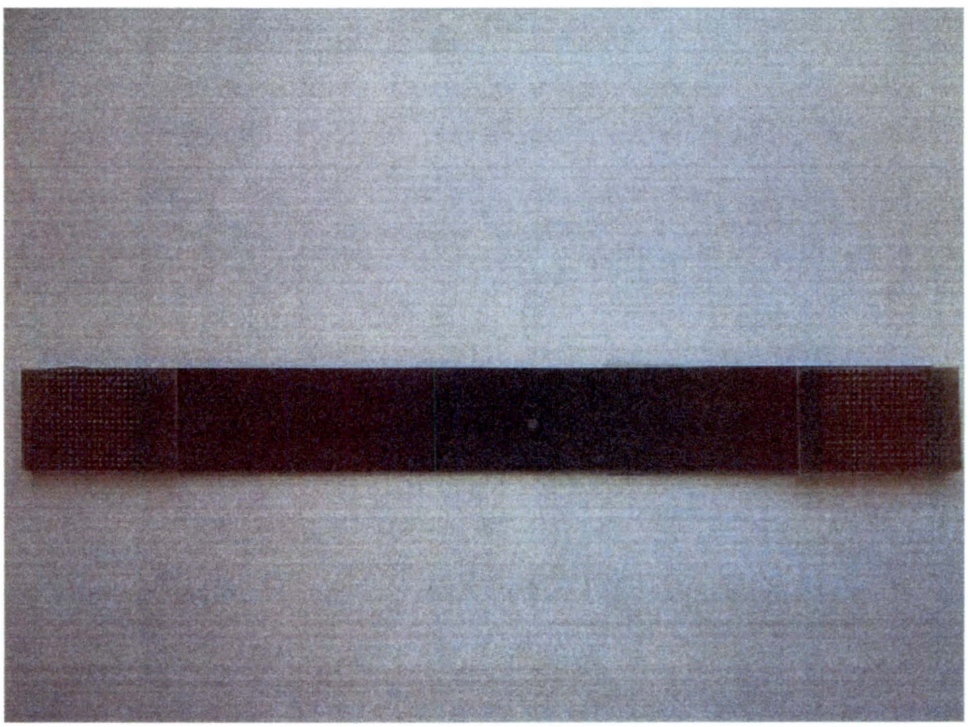

Figure 2.4 A specimen

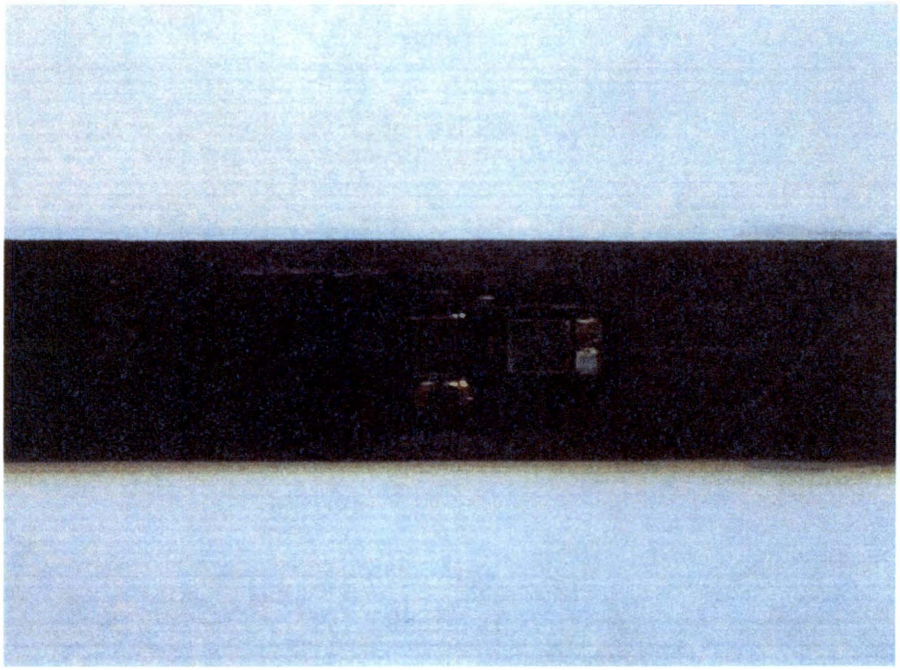

Figure 2.5 Two strain gages on the surface of a specimen

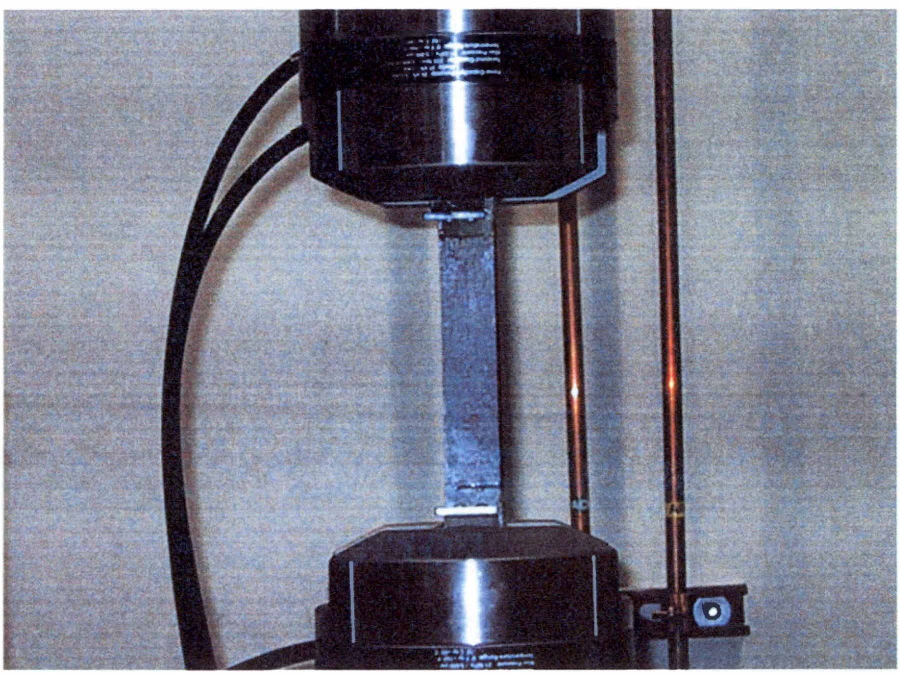

Figure 2.6 A specimen in tensile test

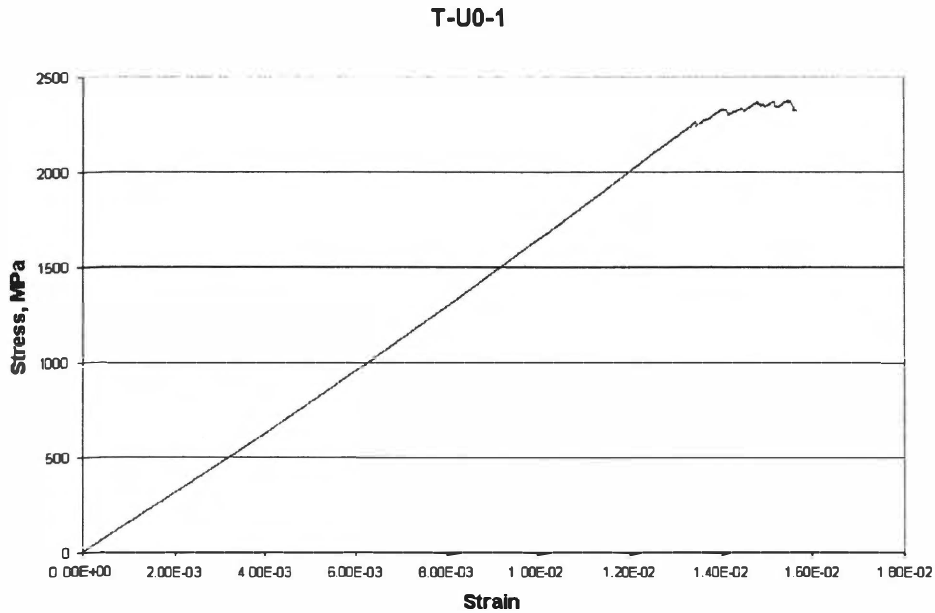

Figure 2.7 Typical stress-strain plot for $[0^\circ]_6$ specimen

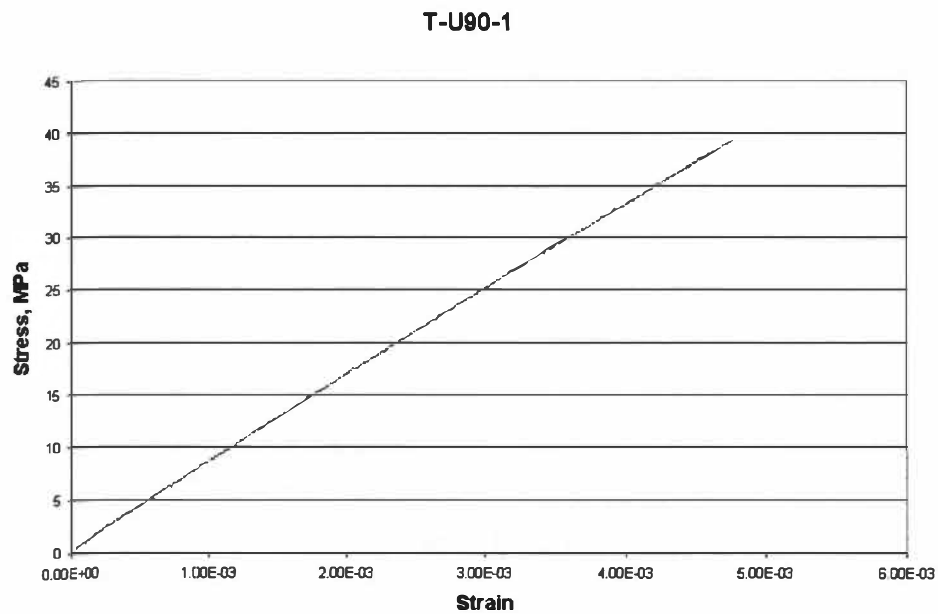

Figure 2.8 Typical stress-strain plot for $[90^\circ]_{12}$ specimen

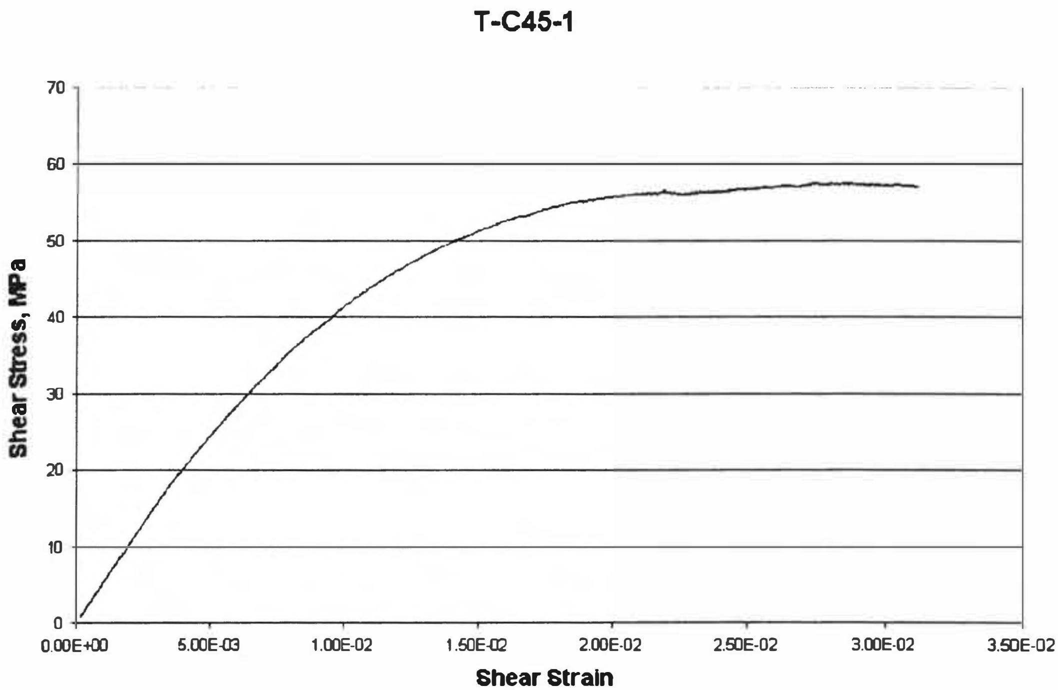

Figure 2.9 Typical stress-strain plot for $[\pm 45^{\circ}]_4$ specimen

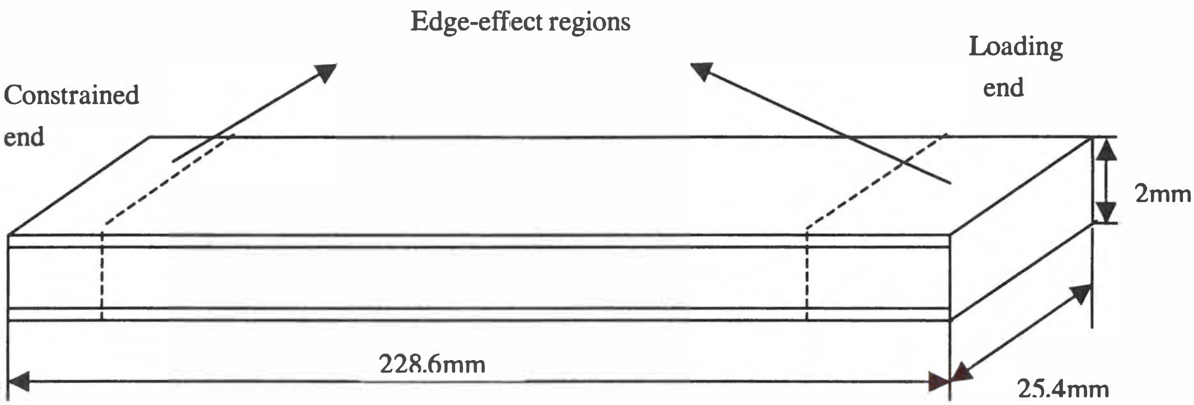

Figure 3.1 Geometric dimensions for computational model

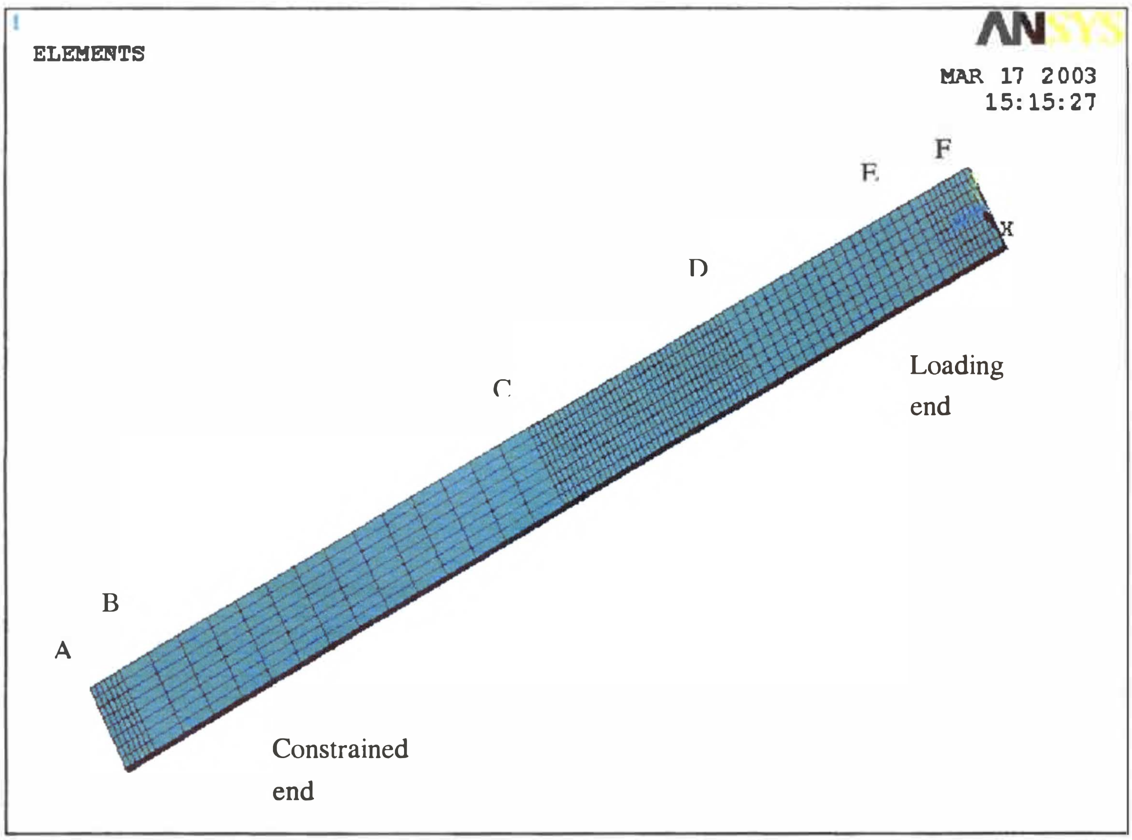

Figure 3.2 Elements of the FEA model

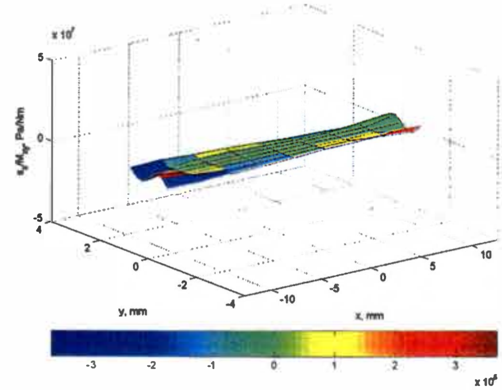

(a) σ_x at z = 0

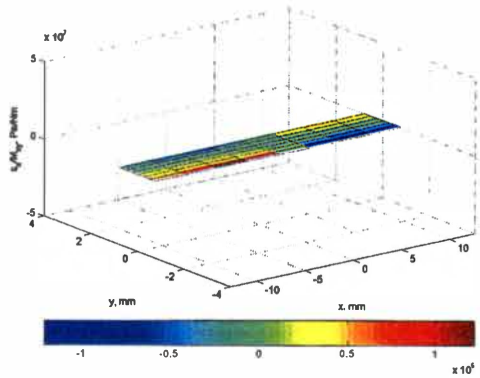

(b) σ_x at z = 1 in

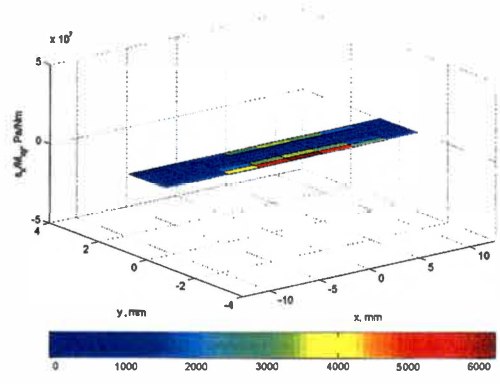

(c) σ_x at z = 3 in

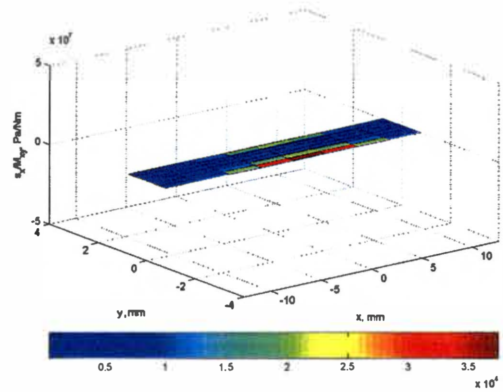

(d) σ_x at z = 4 in

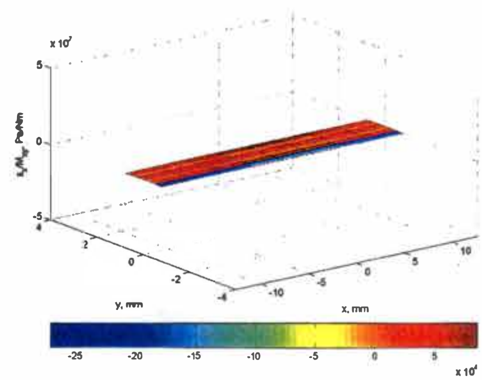

(e) σ_x at z = 4.5 in

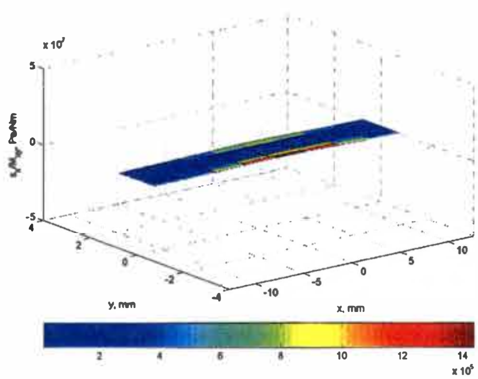

(f) σ_x at z = 6 in

Figure 3.3 Distribution of σ_x at various cross-sections

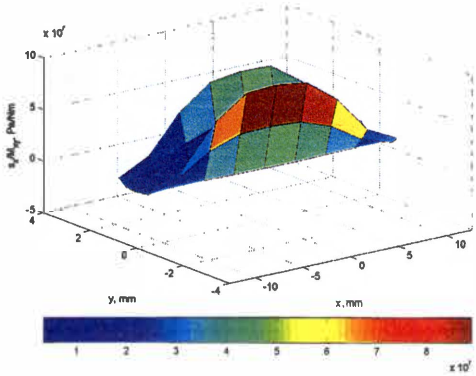

(g) σ_x at z = 8 in

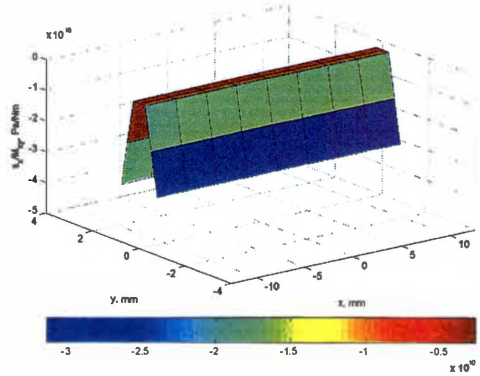

(h) σ_x at z = 9 in

Figure 3.3 Continued

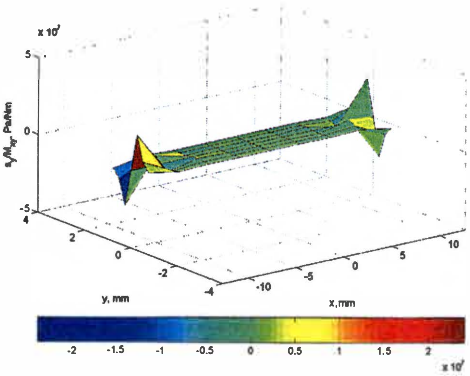

(a) σ_y at z = 0

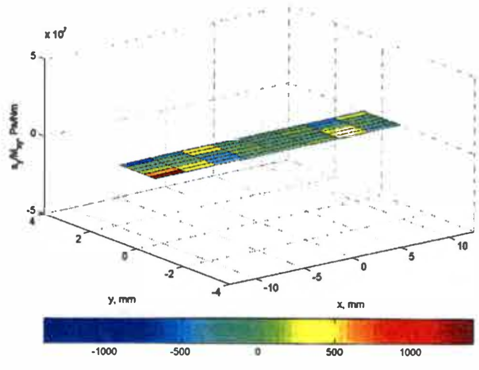

(b) σ_y at z = 1 in

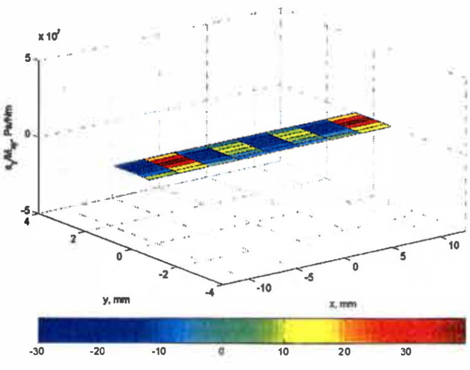

(c) σ_y at z = 3 in

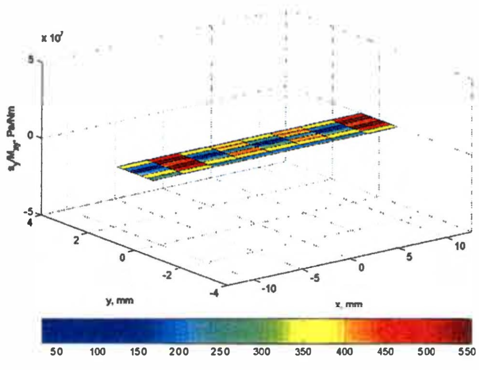

(d) σ_y at z = 4 in

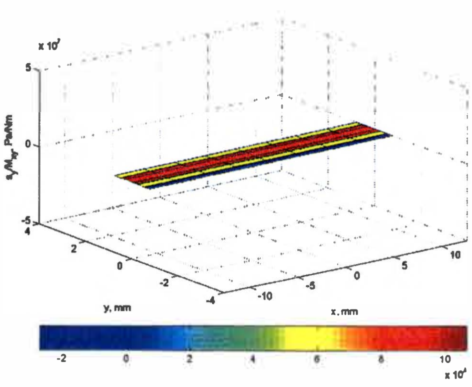

(e) σ_y at z = 4.5 in

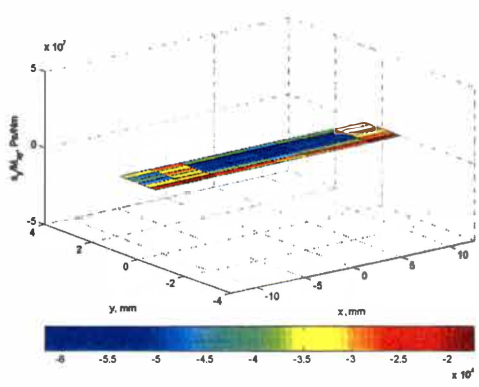

(f) σ_y at z = 6 in

Figure 3.4 Distribution of σ_y at various cross-sections

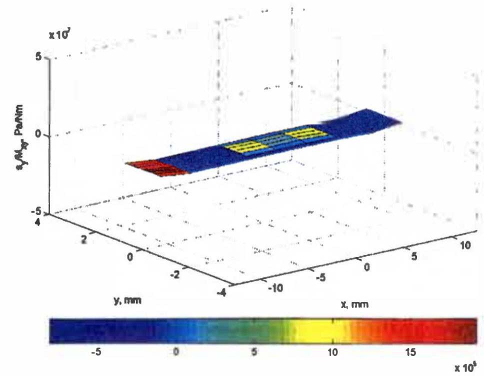

(g) σ_y at z = 8 in

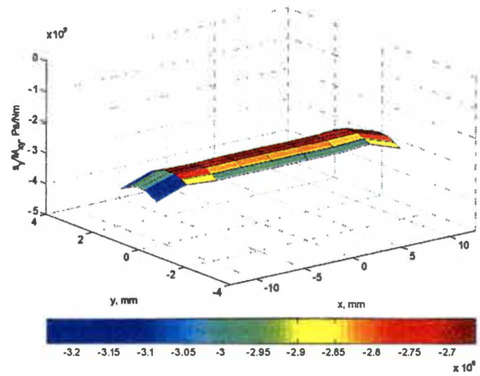

(h) σ_y at z = 9 in

Figure 3.4 Continued

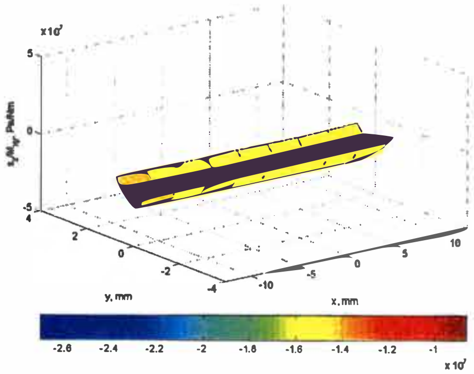

(a) σ_z at z = 0

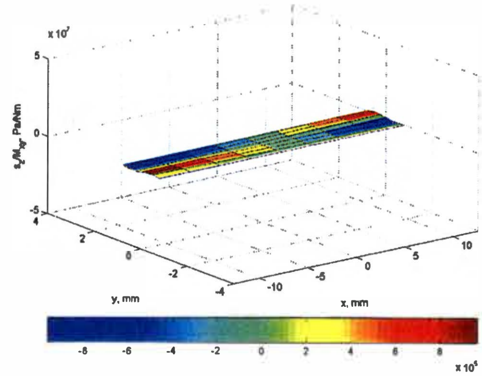

(b) σ_z at z = 1 in

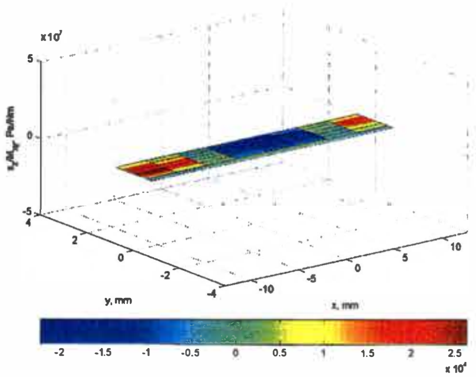

(c) σ_z at z = 3 in

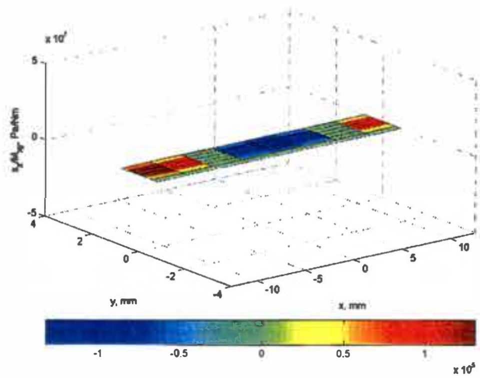

(d) σ_z at z = 4 in

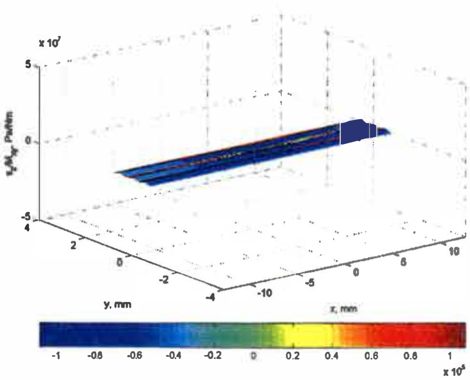

(e) σ_z at z = 4.5 in

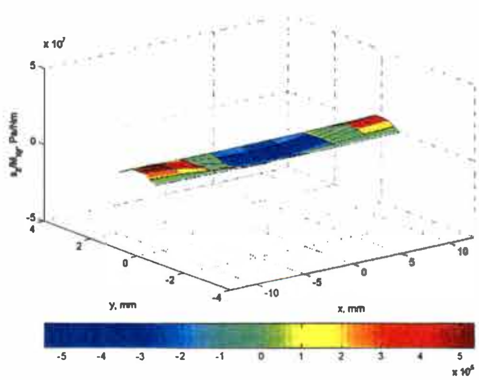

(f) σ_z at z = 6 in

Figure 3.5 Distribution of σ_z at various cross-sections

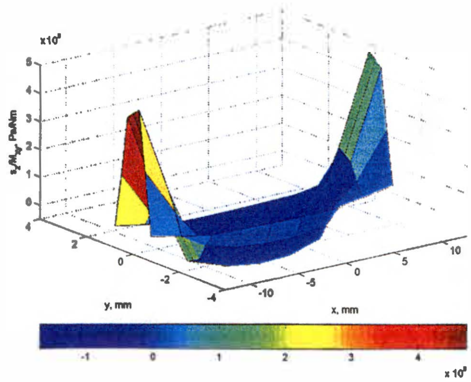

(g) σ_z at z = 8 in

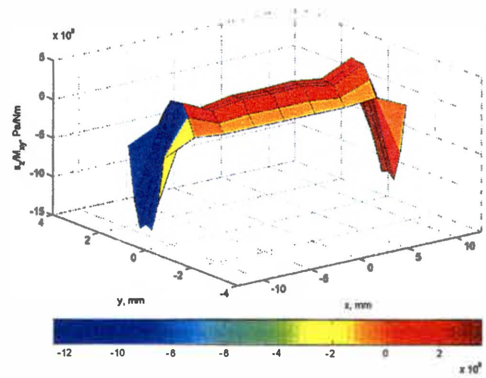

(h) σ_z at z = 9 in

Figure 3.5 Continued

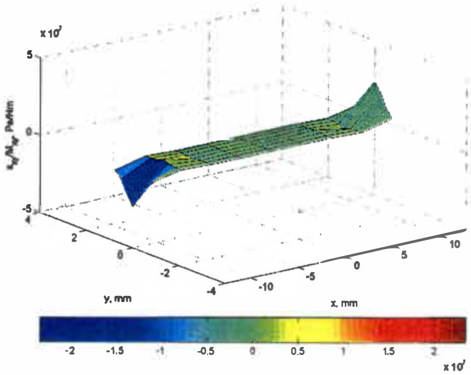

(a) τ_{xy} at z = 0

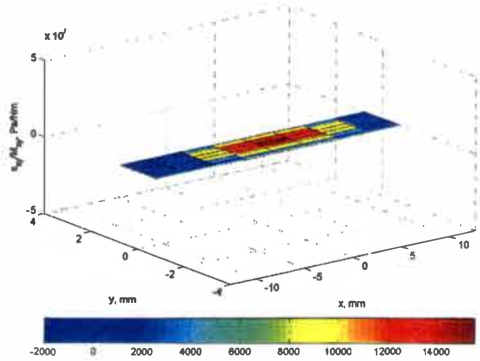

(b) τ_{xy} at z = 1 in

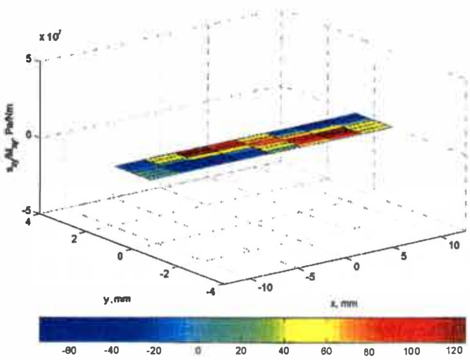

(c) τ_{xy} at z = 3 in

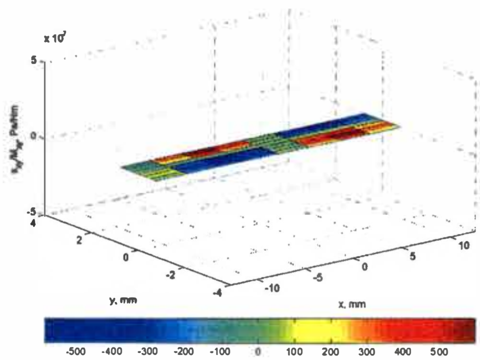

(d) τ_{xy} at z = 4 in

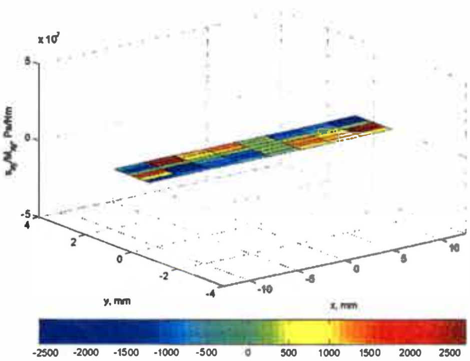

(e) τ_{xy} at z = 4.5 in

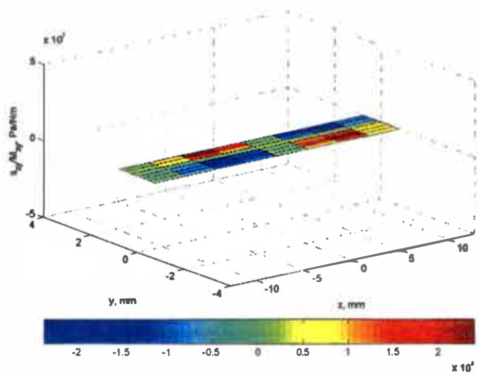

(f) τ_{xy} at z = 6 in

Figure 3.6 Distribution of τ_{xy} at various cross-sections

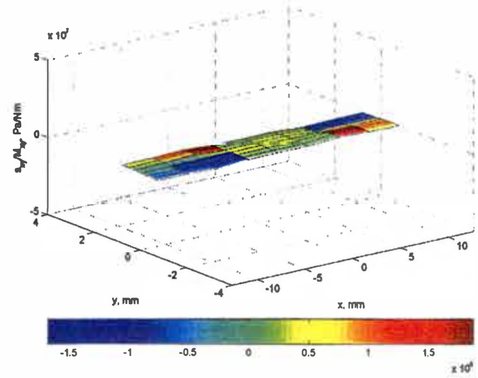

(g) τ_{xy} at z = 8 in

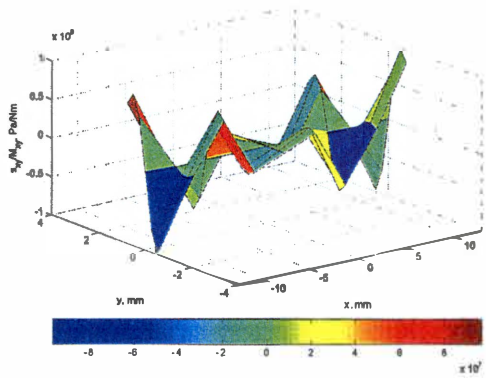

(h) τ_{xy} at z = 9 in

Figure 3.6 Continued

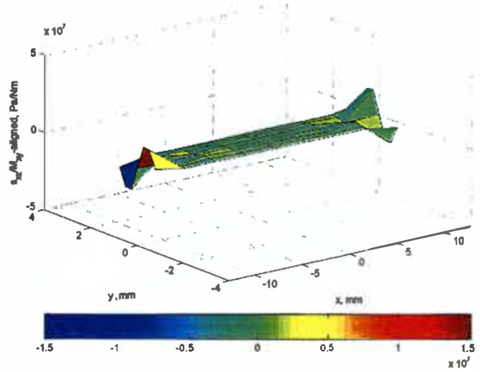

(a) τ_{xz} at z = 0

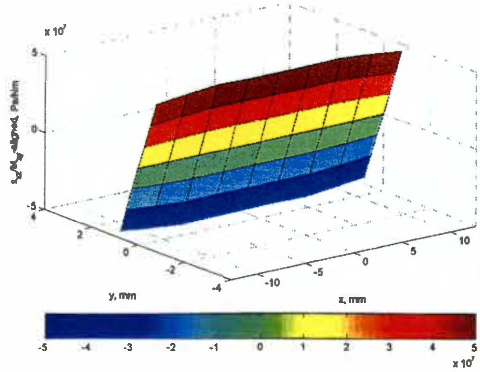

(b) τ_{xz} at z = 1 in

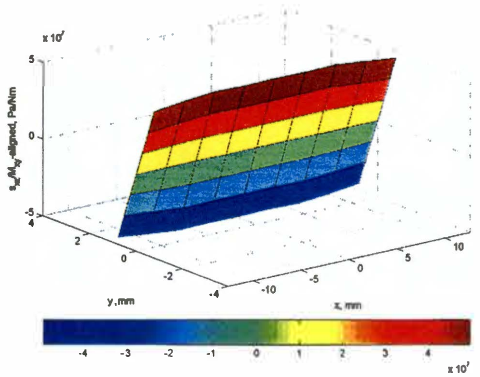

(c) τ_{xz} at z = 3 in

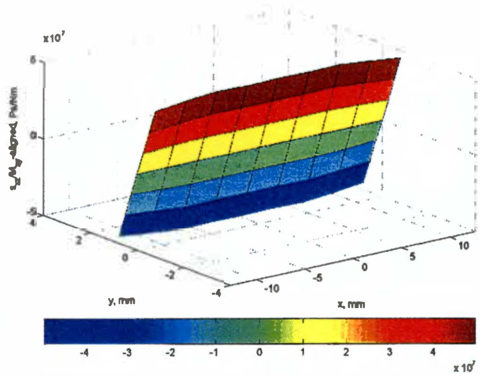

(d) τ_{xz} at z = 4 in

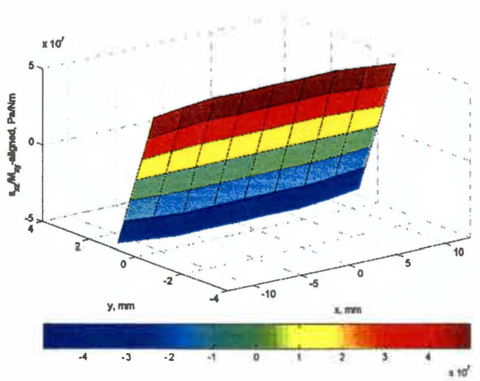

(e) τ_{xz} at z = 4.5 in

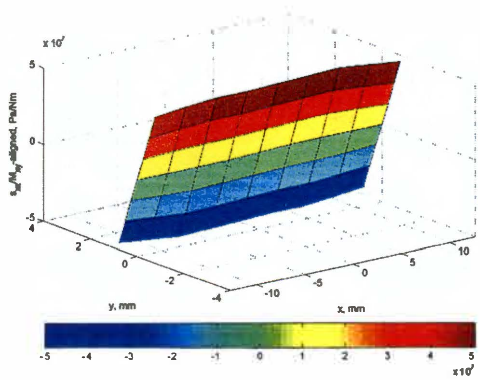

(f) τ_{xz} at z = 6 in

Figure 3.7 Distribution of τ_{xz} at various cross-sections

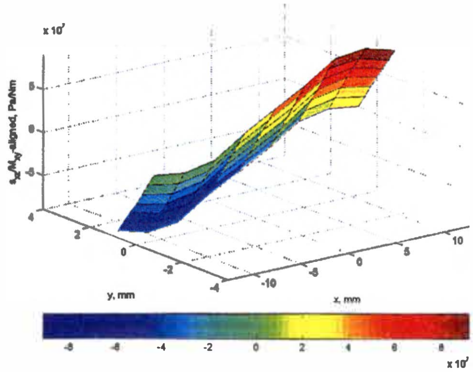

(g) τ_{xz} at z = 8 in

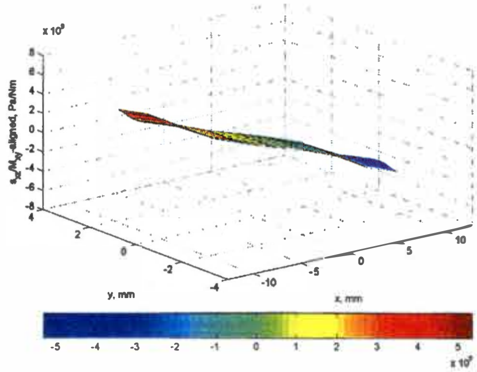

(h) τ_{xz} at z = 9 in

Figure 3.7 Continued

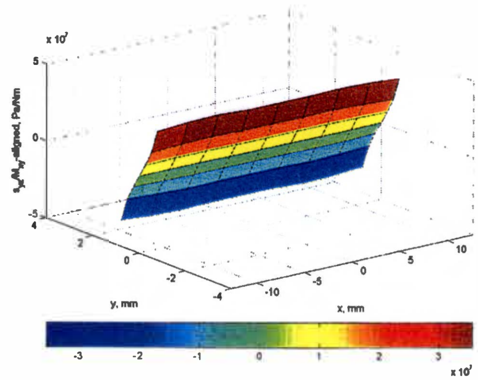

(a) τ_{yz} at z = 0

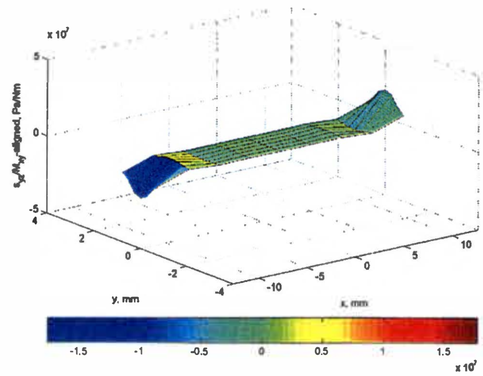

(b) τ_{yz} at z = 1 in

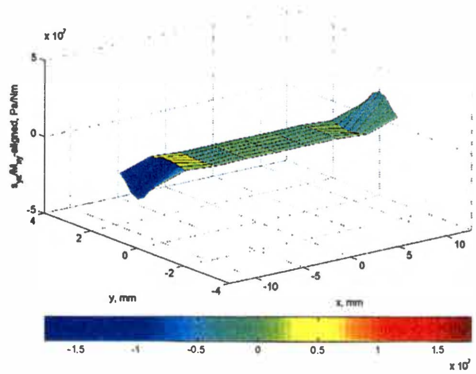

(c) τ_{yz} at z = 3 in

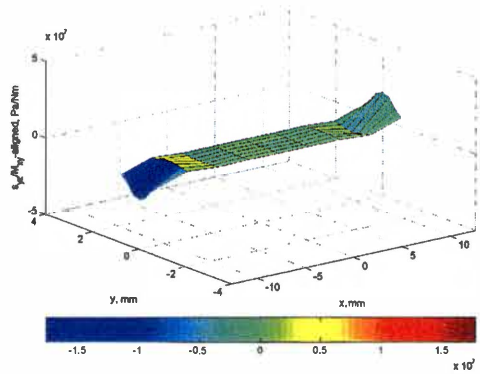

(d) τ_{yz} at z = 4 in

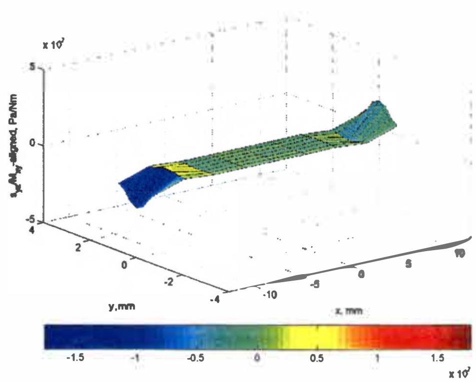

(e) τ_{yz} at z = 4.5 in

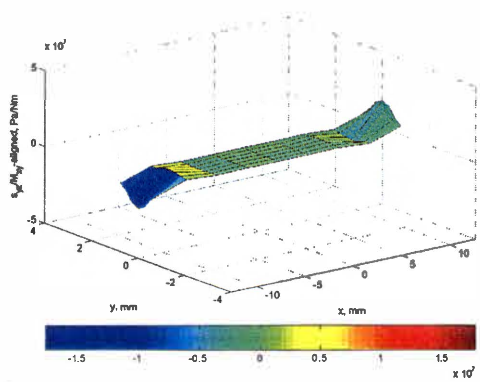

(f) τ_{yz} at z = 6 in

Figure 3.8 Distribution of τ_{yz} at various cross-sections

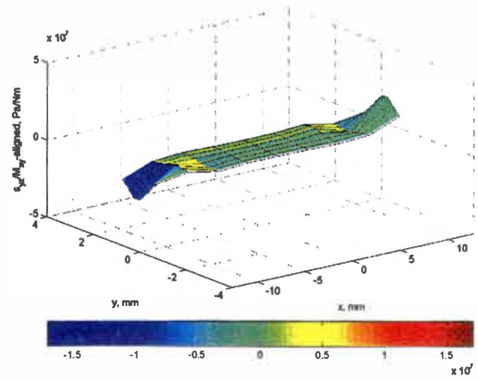

Figure 3.8(g) τ_{yz} at z = 8 in

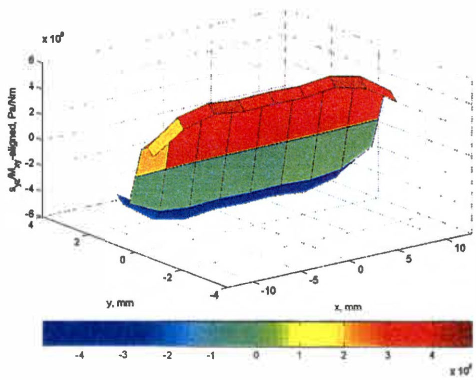

Figure 3.8(h) τ_{yz} at z = 9 in

Figure 3.8 Continued

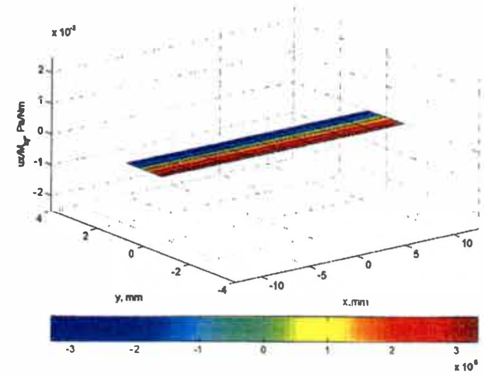
(a) u_x at z = 0

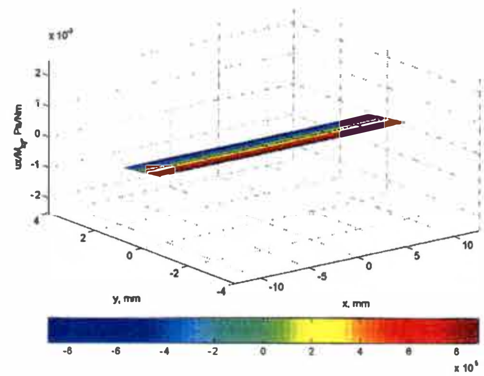
(b) u_x at z = 1 in

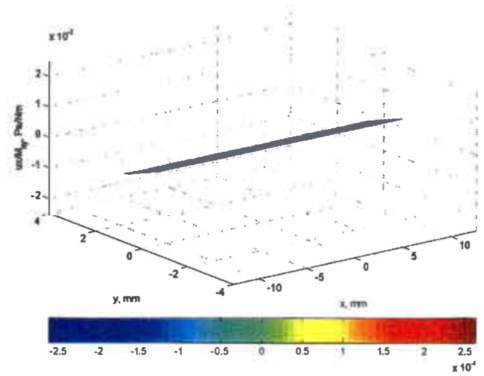
(c) u_x at z = 3 in

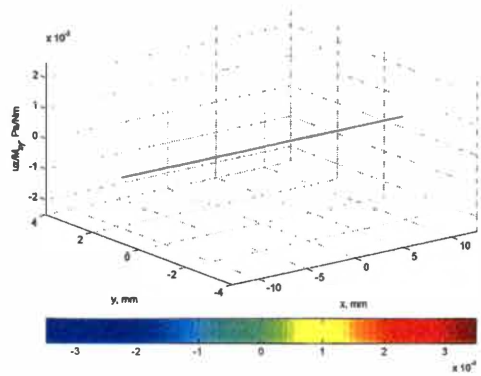
(d) u_x at z = 4 in

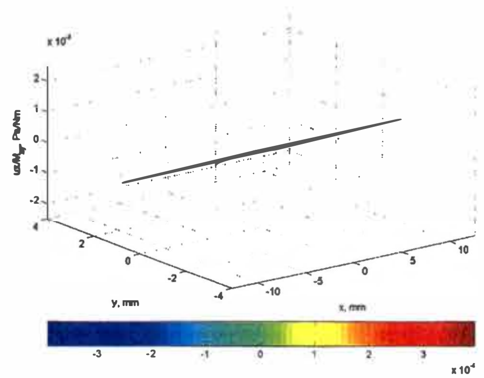
(e) u_x at z = 4.5 in

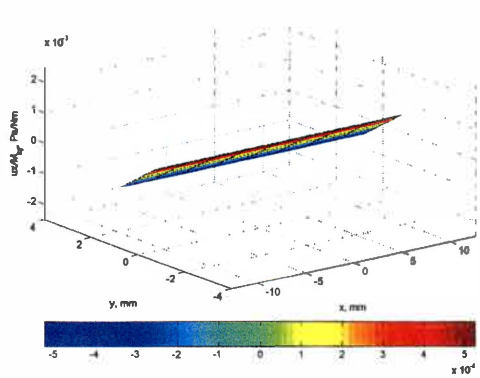
(f) u_x at z = 6 in

Figure 3.9 Distribution of u_x at various cross-sections

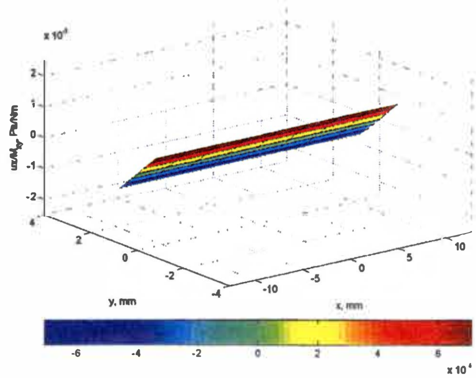

(g) u_x at z = 8 in

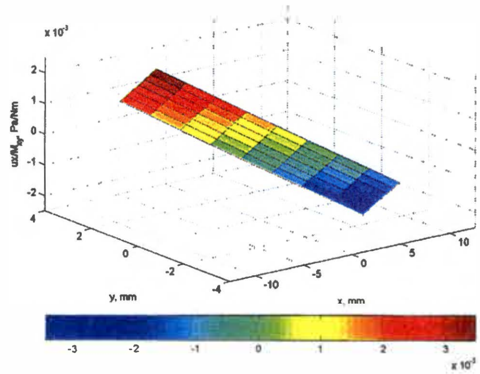

(h) u_x at z = 9 in

Figure 3.9 Continued

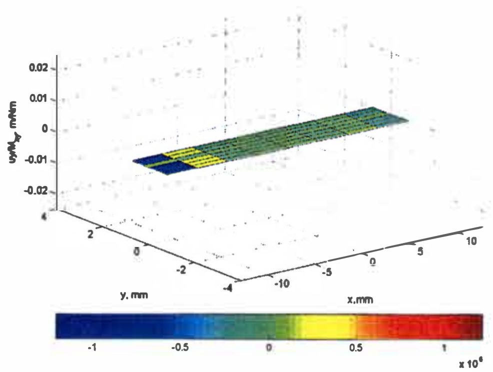

(a) u_y at z = 0 in

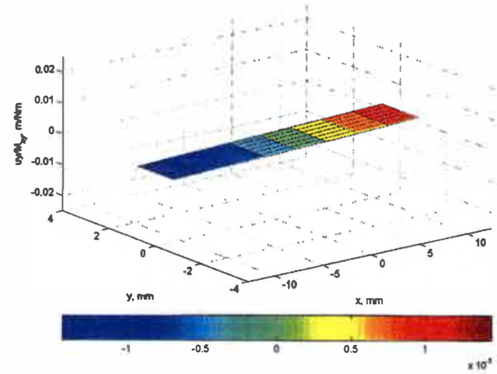

(b) u_y at z = 1 in

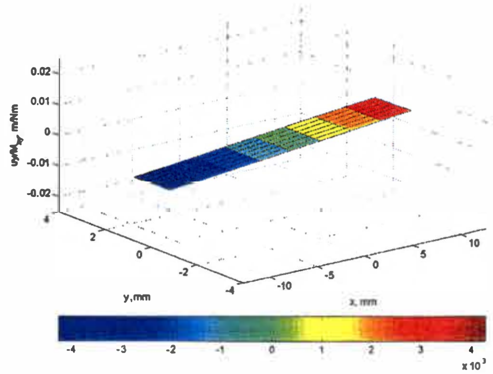

(c) u_y at z = 3 in

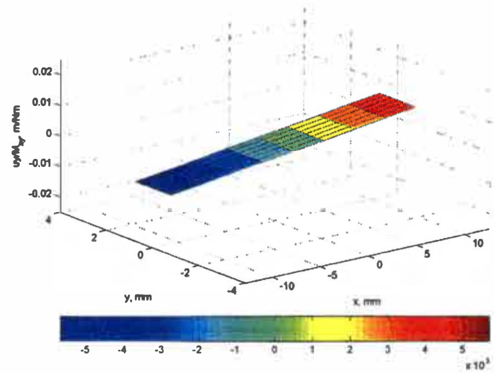

(d) u_y at z = 4 in

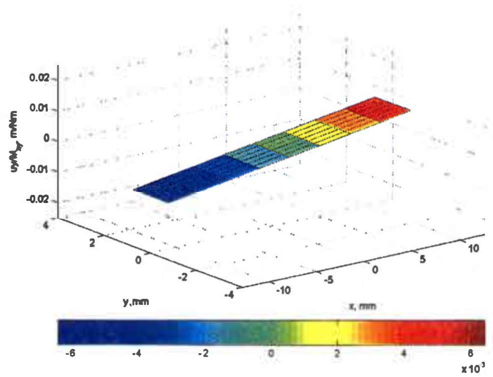

(e) u_y at z = 4.5 in

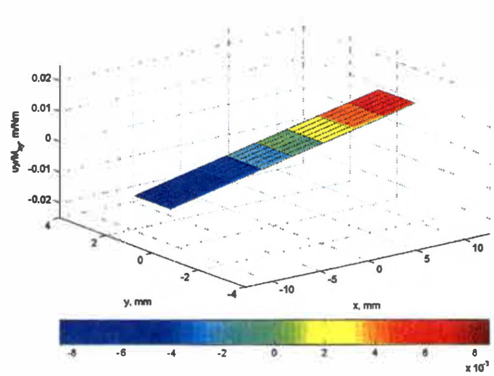

(f) u_y at z = 6 in

Figure 3.10 Distribution of u_y at various cross-sections

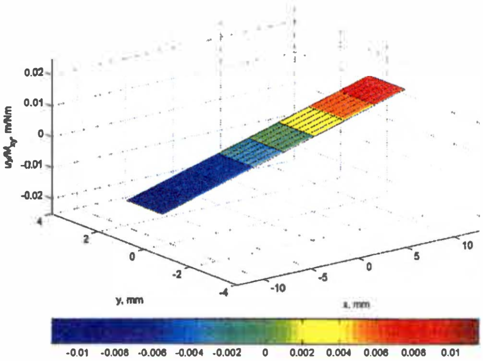

(g) u_y at $z = 8$ in

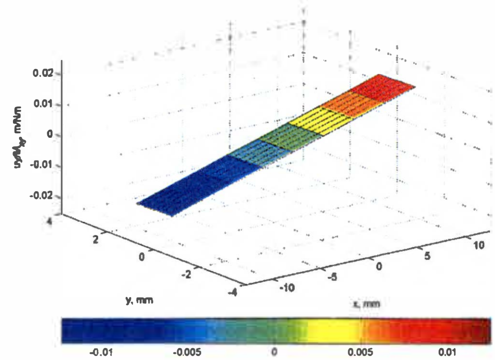

(h) u_y at $z = 9$ in

Figure 3.10 Continued

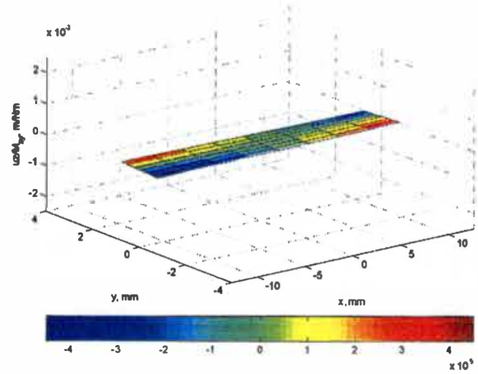

(a) u_z at z = 0

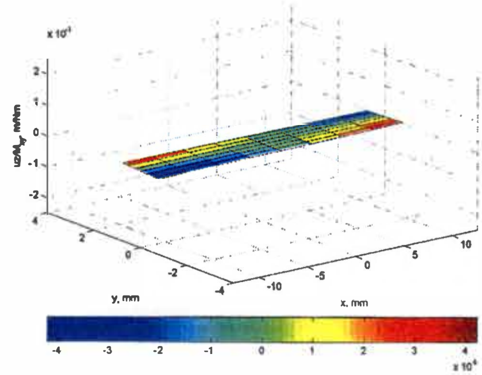

(b) u_z at z = 1 in

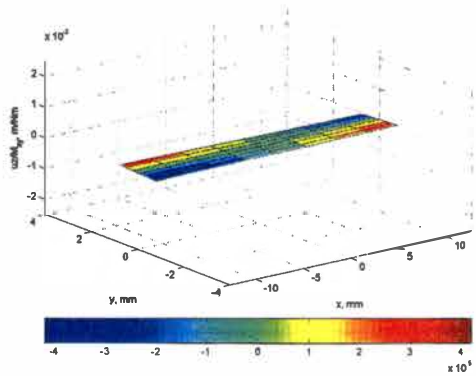

(c) u_z at z = 3 in

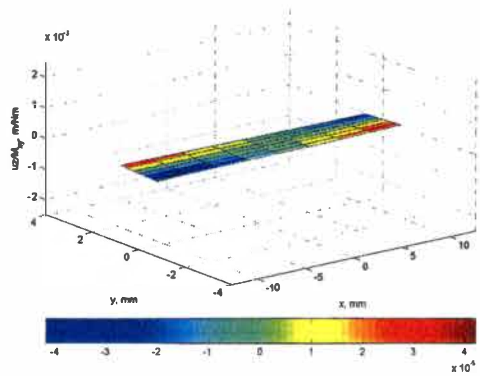

(d) u_z at z = 4 in

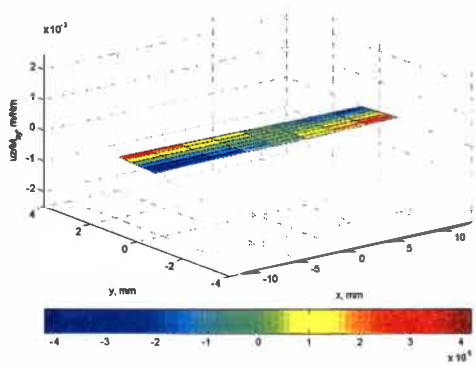

(e) u_z at z = 4.5 in

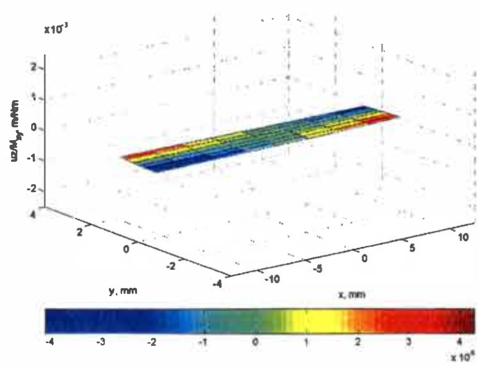

(f) u_z at z = 6 in

Figure 3.11 Distribution of u_z at various cross-sections

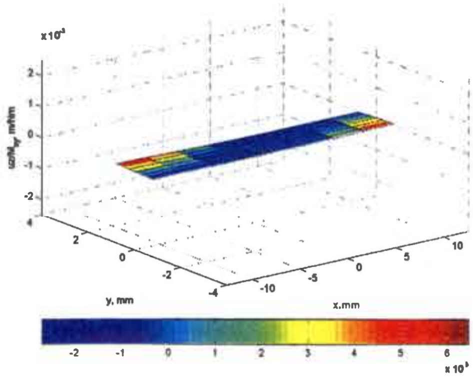

Figure 3.11(g) u_z at z = 8 in

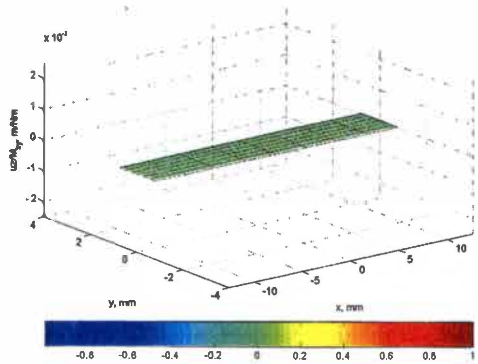

Figure 3.11(h) u_z at z = 9 in

Figure 3.11 Continued

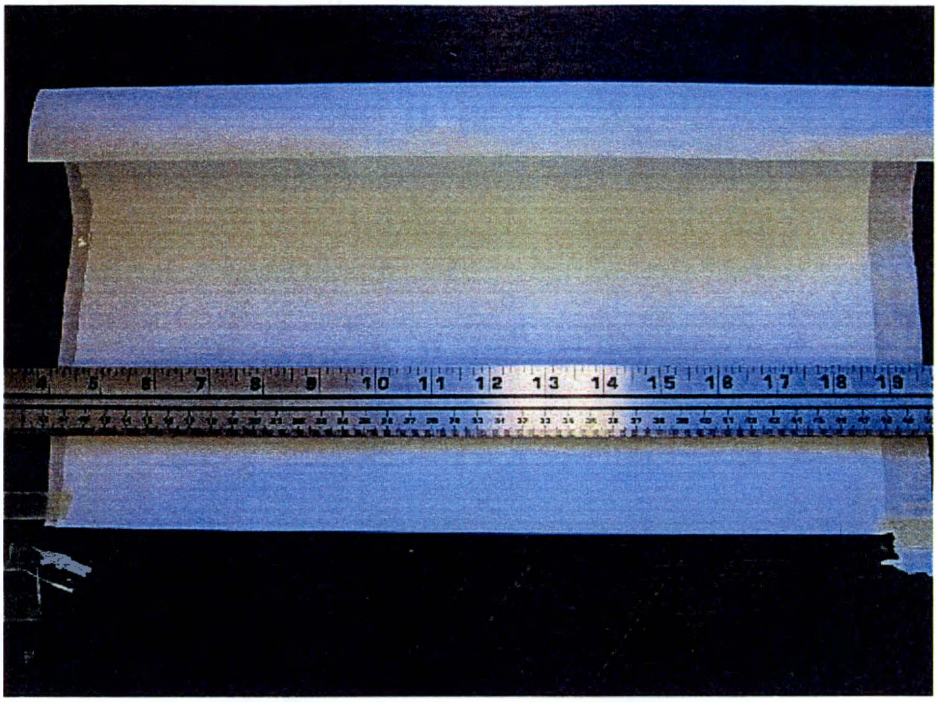

Figure 4.1 Cutting Teflon film

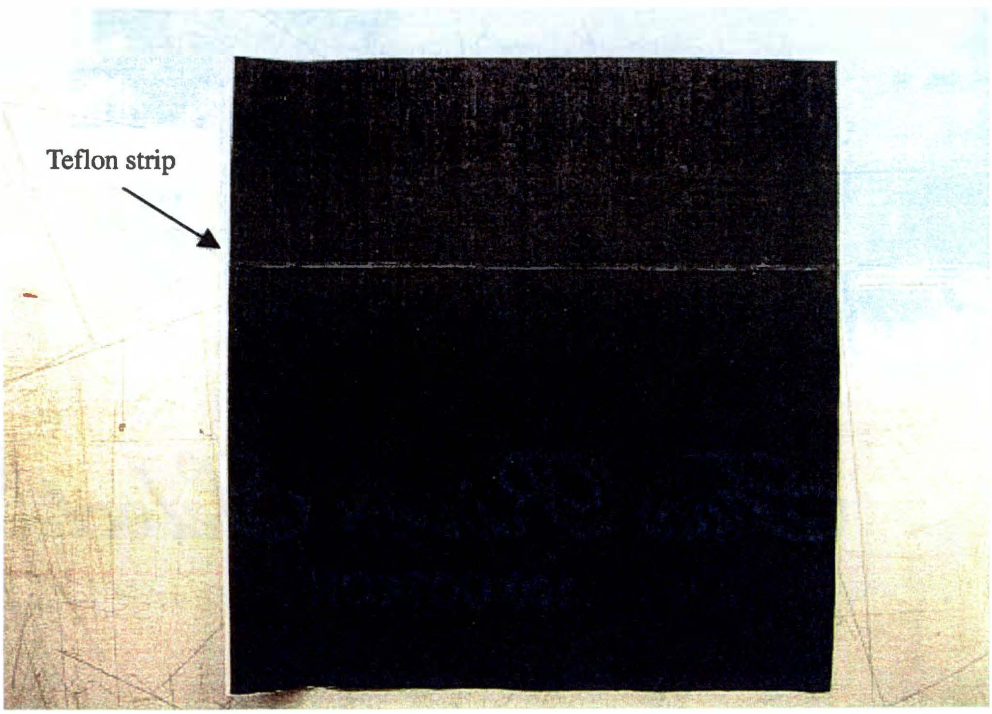

Figure 4.2 AS4/3501-6 prepreg with a Teflon film strip

Figure 4.3 Hewlett Packard 43804N X-Ray system

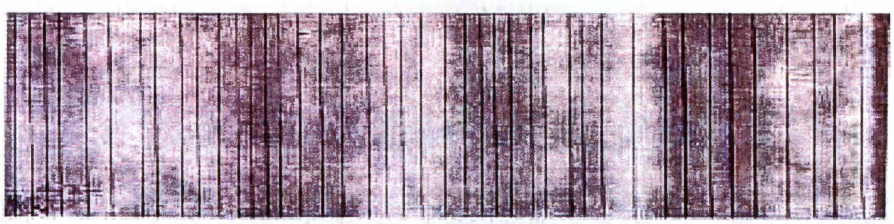

Figure 4.4 An X-radiograph for a specimen after tensile test

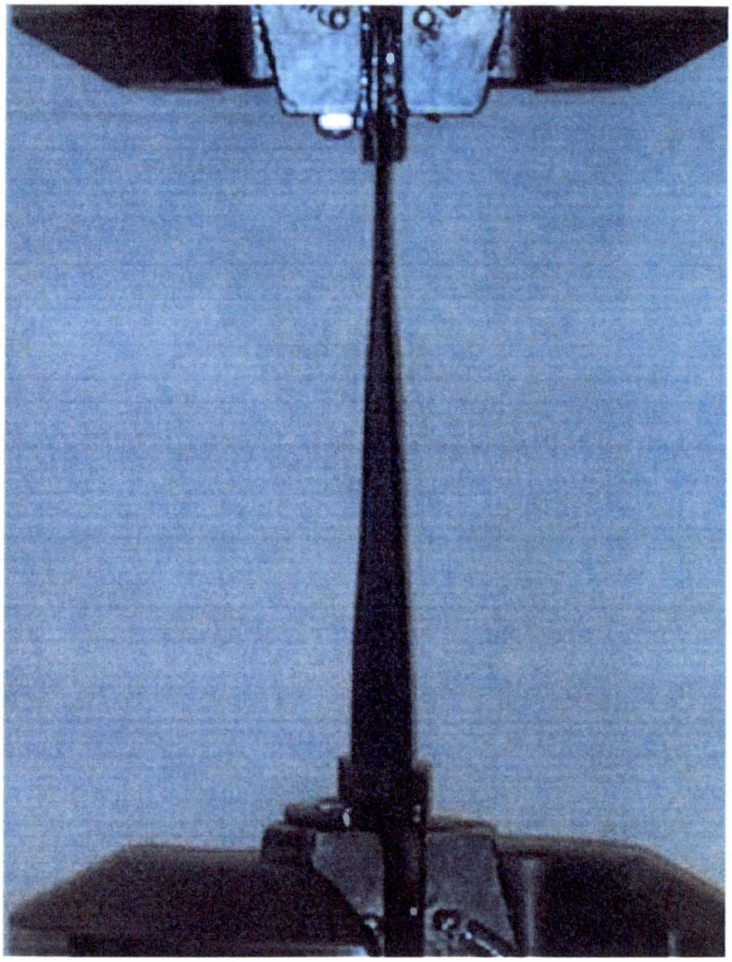

Figure 4.5 A specimen in torsion test

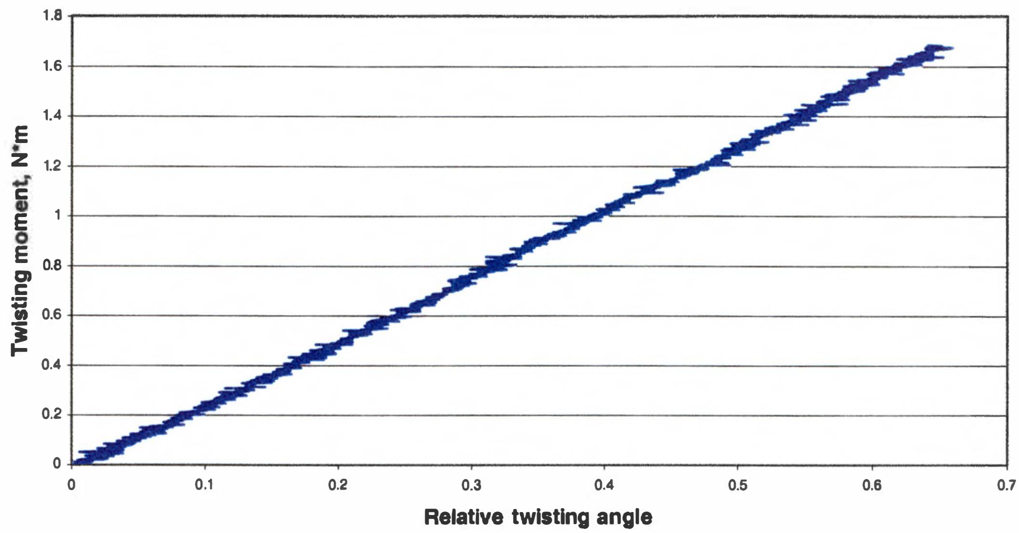

Figure 4.6 Typical twisting-moment vs. angle (φ / l) plot

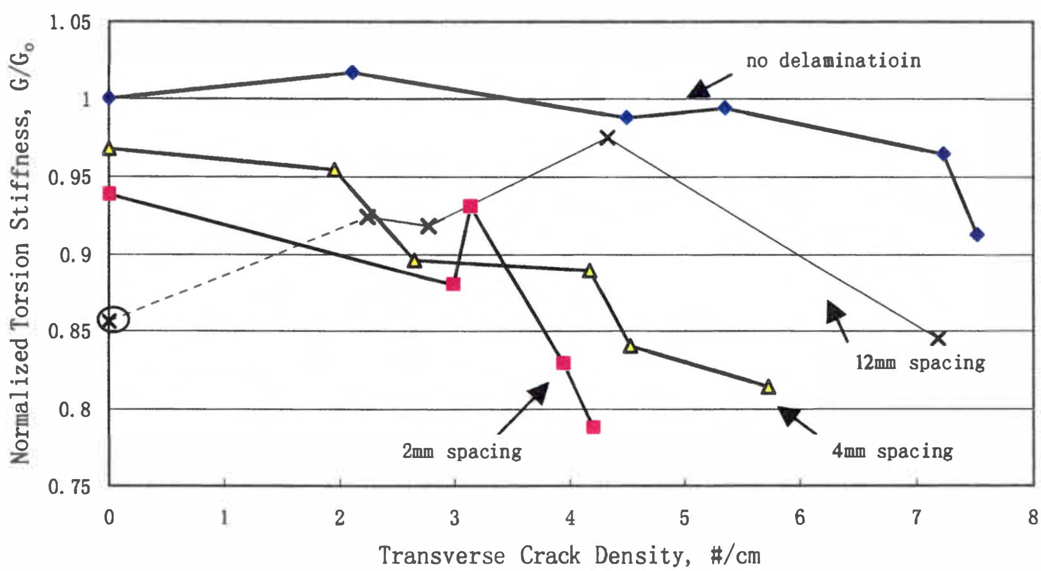

Figure 4.7 Torsional stiffness degradation vs. transverse crack density for various delamination spacings

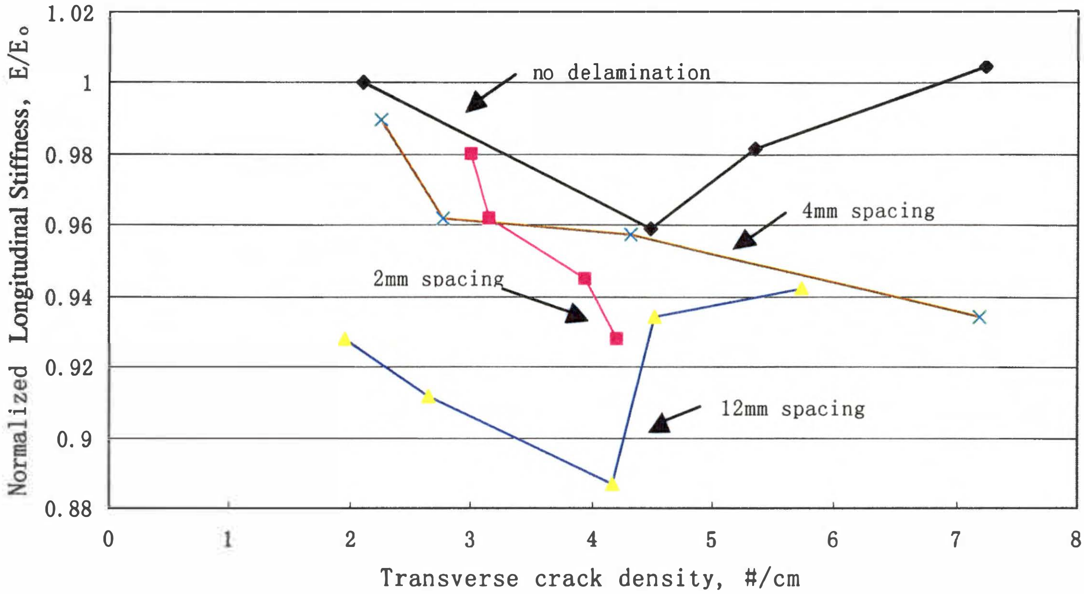

Figure 4.8 Longitudinal stiffness degradation vs. internal damage at various delamination spacings

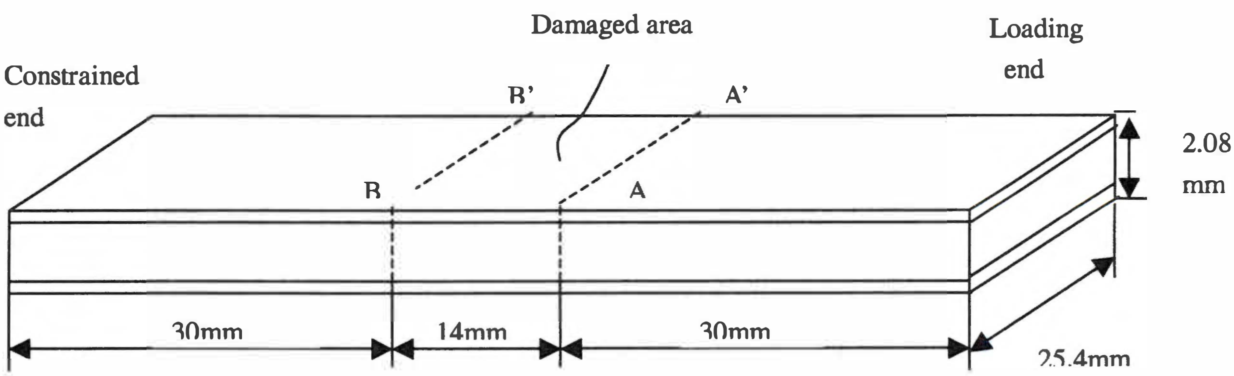

Figure 5.1 Configuration of computational model

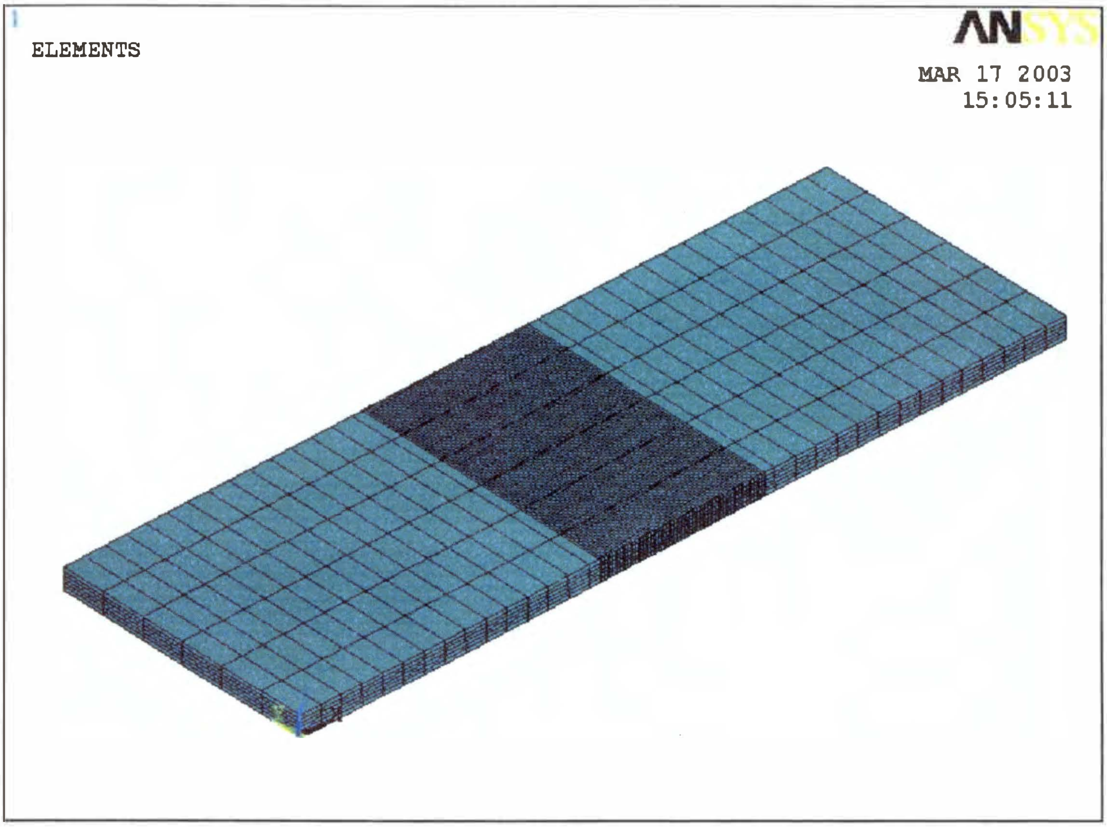

Figure 5.2 Elements of the FEA model

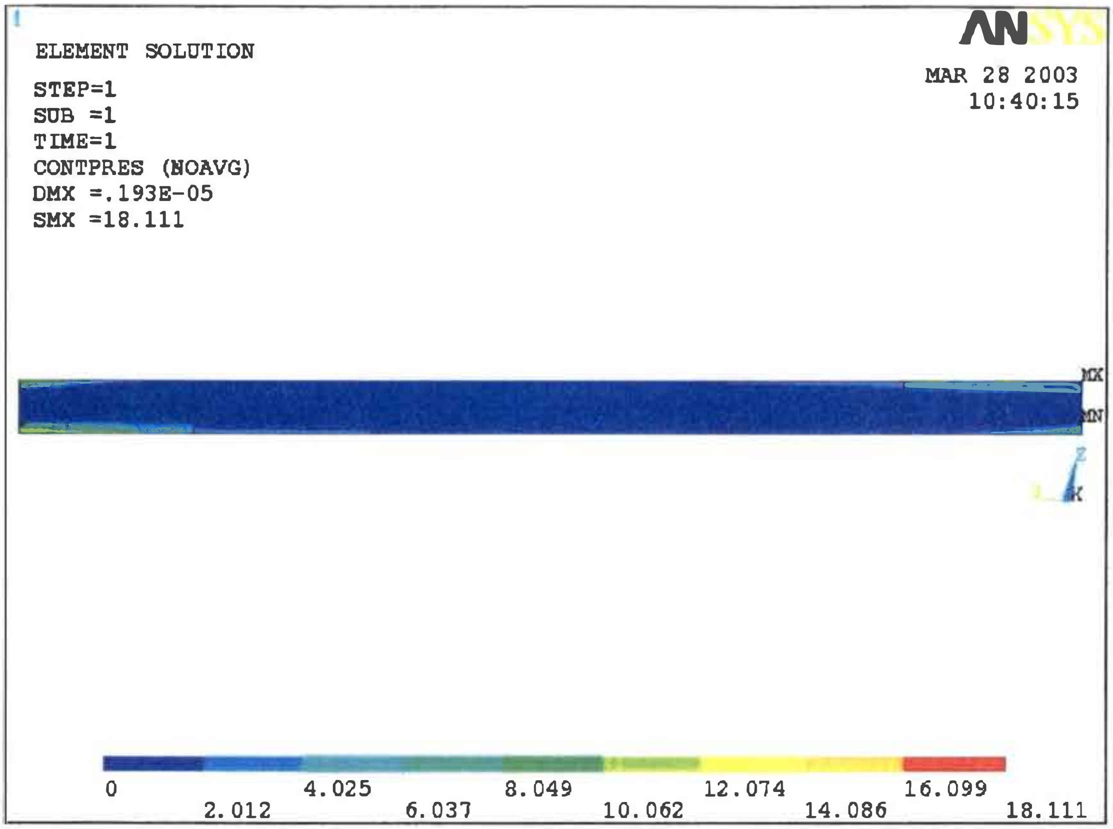

Figure 5.3 Typical distribution of compressive stress on crack surface

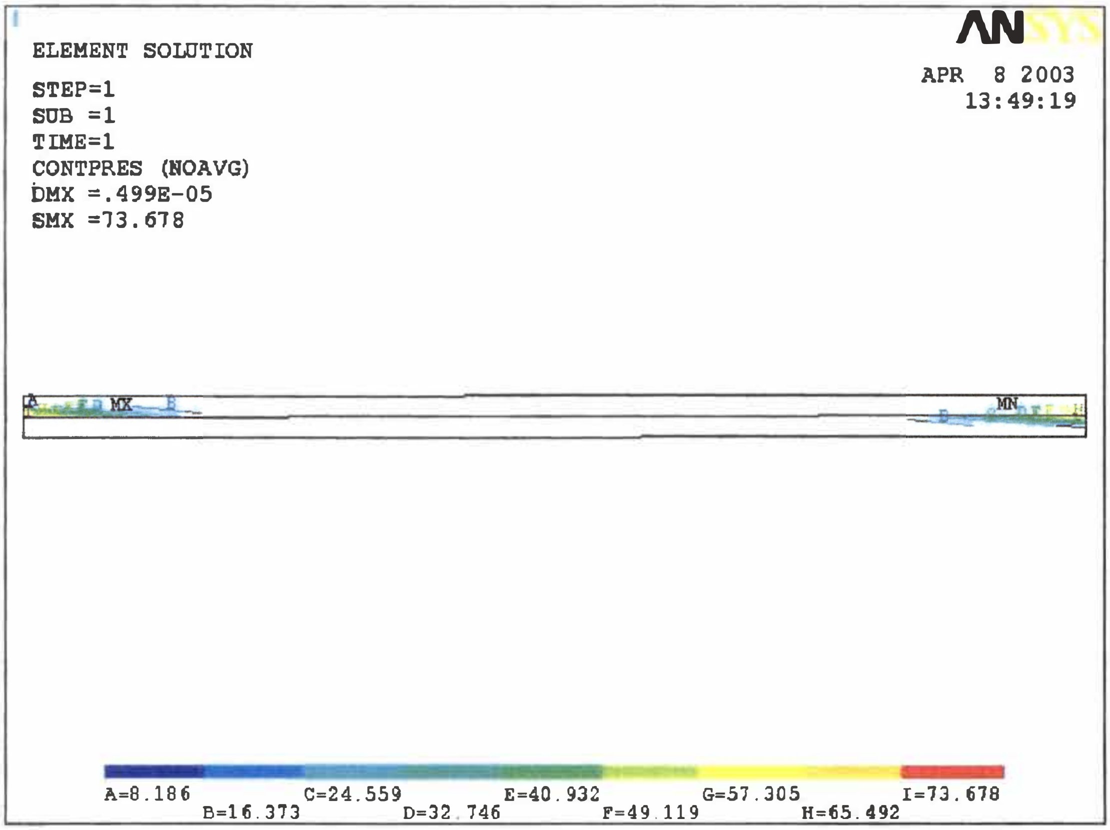

Figure 5.4 Typical distribution of compressive stress on delamination surface

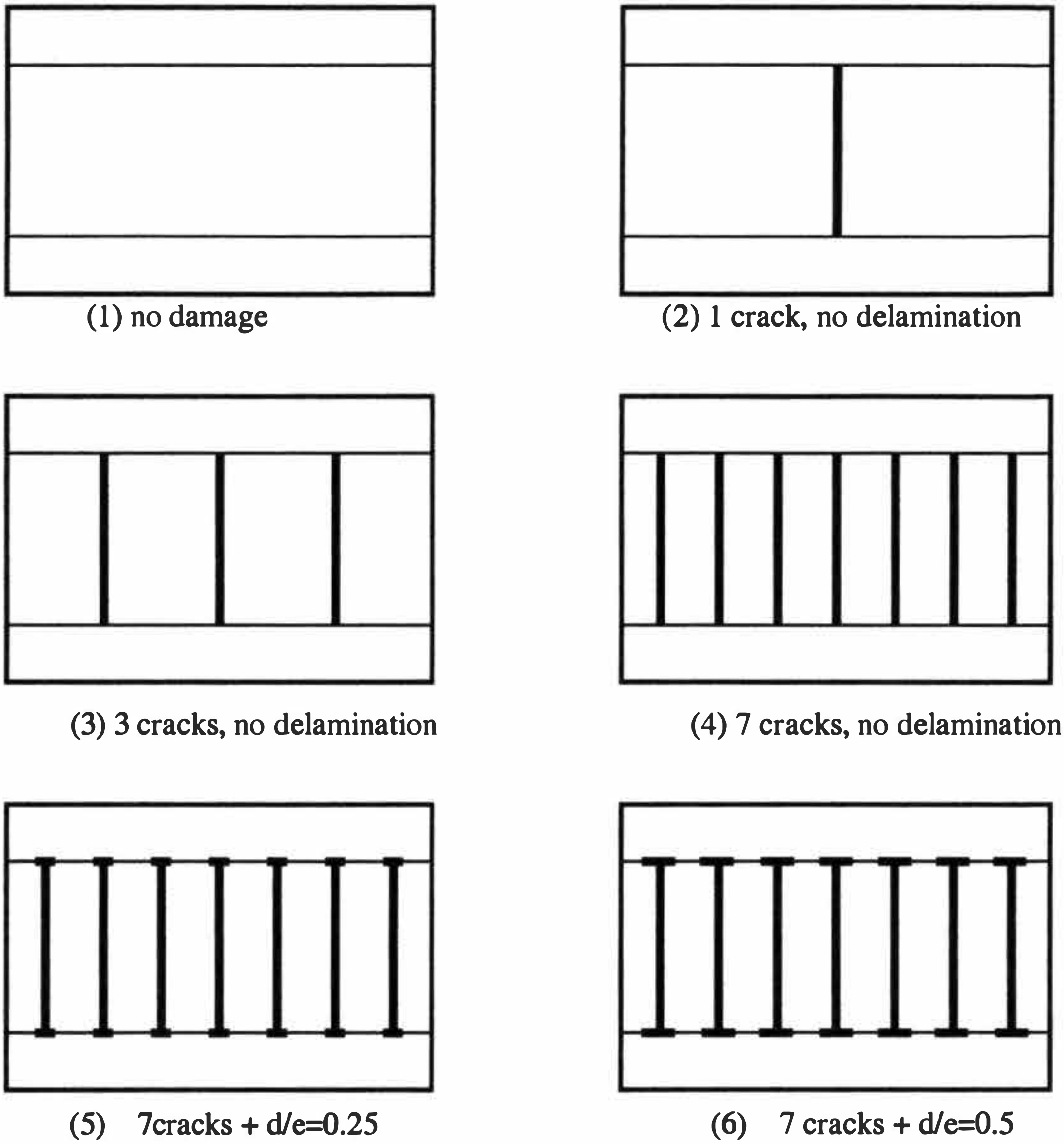

Figure 5.5 A schematic drawing detailing the configurations of seven sequential damage states

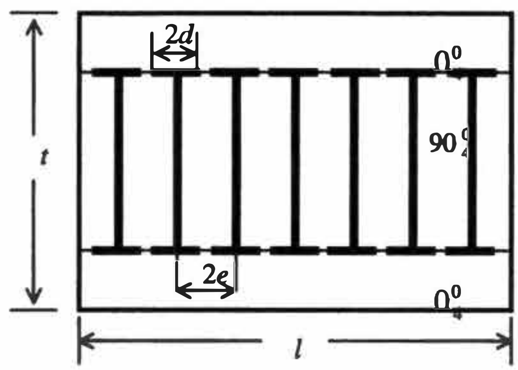

(7) 7 cracks + d/e=0.75

Figure 5.5 Continued

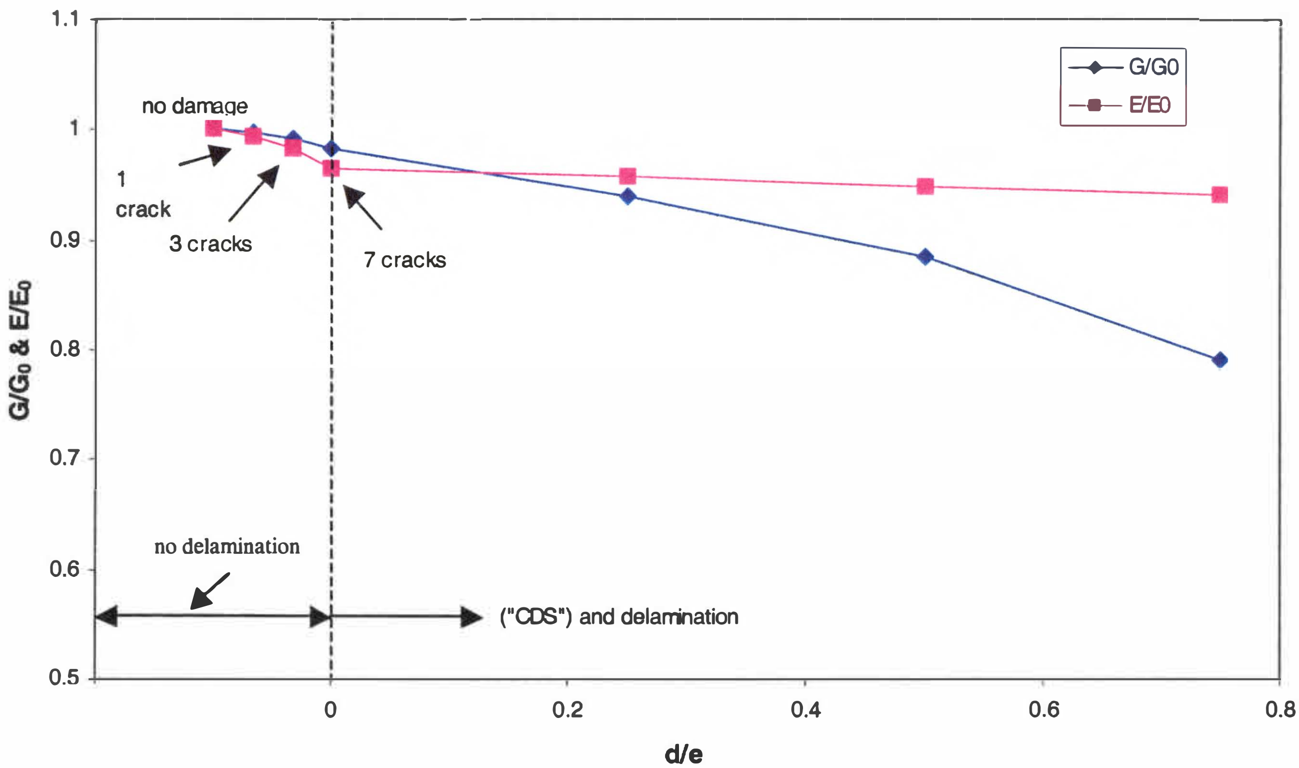

Figure 5.6 Normalized torsional and tensile stiffnesses (E/E_0 and G/G_0, respectively) vs. damage extent (density of transverse cracks and delamination size)

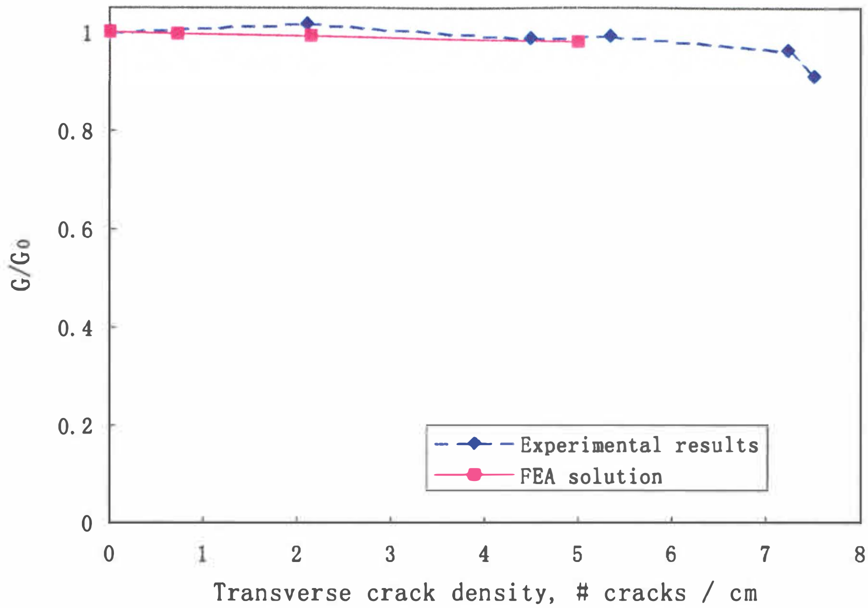

(a) No-delamination set

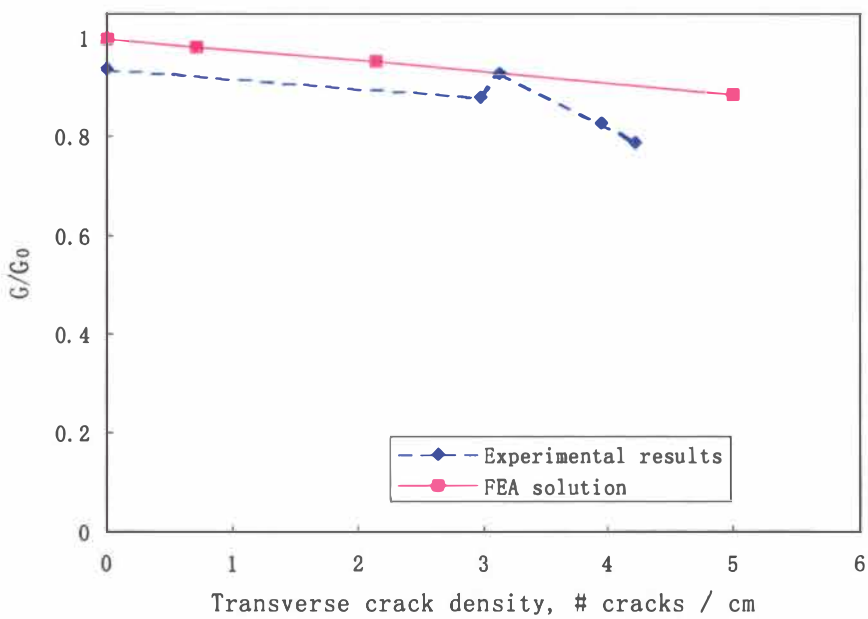

(b) 2mm-spaced delamination set

Figure 5.7 FEA solution and experimental results for torsional stiffness degradation

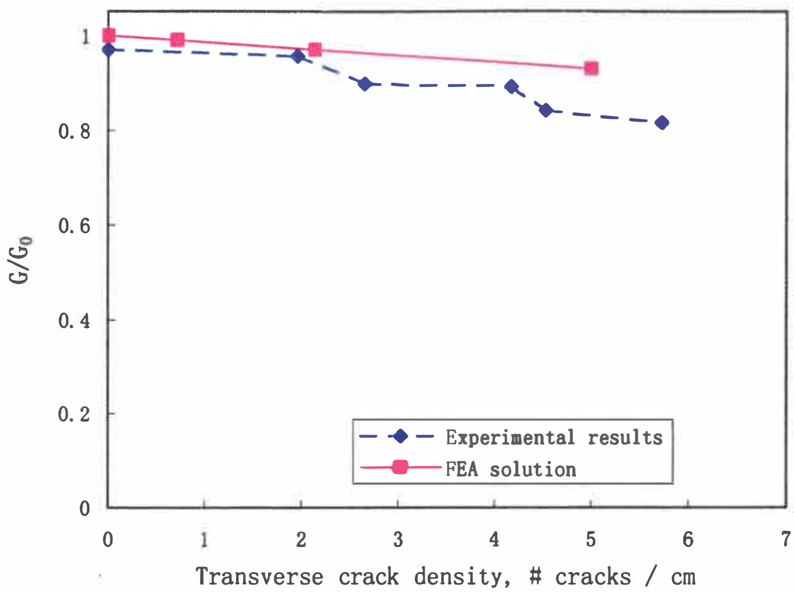

(c) 4mm-spaced delamination set

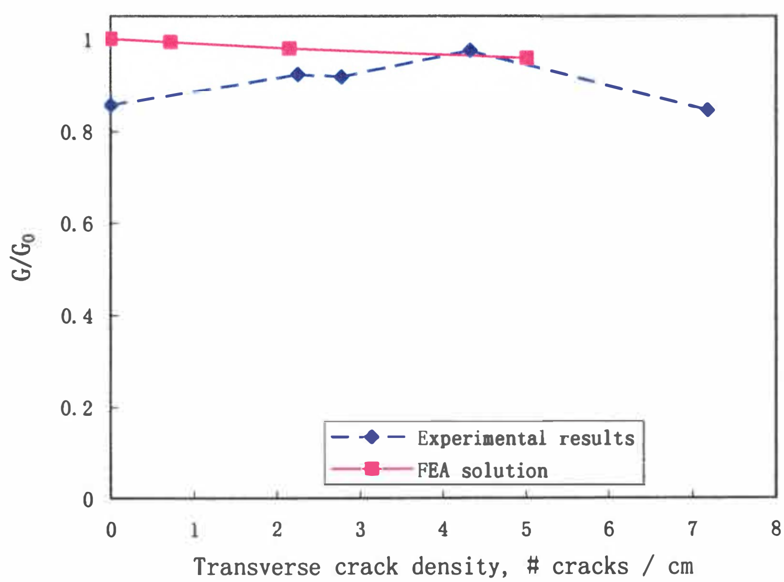

(d) 12mm-spaced delamination set

Figure 5.7 Continued

VITA

Rui Tang was born in Shanghai, China, on 25 October, the son of Wenming Tang and Tingxiu Bai. After completing his work at Shenyang Experimental High School, he went on to the Beihang University, also known as Beijing University of Aeronautics and Astronautics, where he studied Engineering Mechanics and received his Bachelor of Science in July 1999. For the next two years he work for Guangzhou Aircraft Maintenance Engineering Corporation, Ltd. He entered the Graduate School at the University of Tennessee at Knoxville.

This thesis was typed by the author.